Heliyon 10 (2024) e30325

Contents lists available at ScienceDirect

Heliyon

journal homepage: www.cell.com/heliyon

Research article

In-depth analysis of embedded-type structures of $Ni_xMg_{4-x}Al$ LDO-composited catalysts and the impacts on glycerol conversion under a base- and H_2-free condition

Darine Denala [a,b], Wutthikrai Busayaporn [c], Wantana Klysubun [c], Sirirat Jitkarnka [a,b,*]

[a] The Petroleum and Petrochemical College, Chulalongkorn University, Phayathai Road, Pathumwan, Bangkok, 10330, Thailand
[b] Center of Excellence on Petrochemical and Materials Technology, Chulalongkorn University, Phayathai Road, Pathumwan, Bangkok, 10330, Thailand
[c] Synchrotron Light Research Institute, 111 University Avenue, Suranaree, Muang District, Nakhon Ratchasima, 30000, Thailand

ARTICLE INFO

Keywords:
Glycerol
Bio-based chemicals
Lactic acid
1,2-Propanediol
Sustainability

ABSTRACT

Core-shell composite catalysts composing of $AgO@SnO_2$/ZSM-5 embedded by $Ni_xMg_{4-x}AlO$ LDOs with various Ni/Mg ratios were characterized and tested for the activity on the conversion of glycerol to valuable chemicals under a base-free and external H_2-free condition. As a result, the catalytic performance of an embedded composite was found greater than that of its individual constituents, owing to the synergy between a $Ni_xMg_{4-x}AlO$ lodge and embedded $AgO@SnO_2$/ZSM-5. The highest yield of 1,2-propanediol and lactic acid was achieved at the Ni/Mg ratio of 0.2/3.8. $Ni_xMg_{4-x}AlO$ lodges were found to simultaneously drive glycerol dehydration to acetol and glycerol reforming, driven by Ni sites, forming *in-situ* H_2 that enhances 1,2-propanediol formation whereas the $AgO@SnO_2$/ZSM-5 clusters governed acetol oxidation and Cannizzaro reaction that led to the formation of lactic acid. At a high Ni/Mg ratio, the $Ni_xMg_{4-x}AlO$ lodges completely covered $AgO@SnO_2$/ZSM-5 clusters entirely, resulting in the suppression of lactic acid yield due to over-oxidation.

1. Introduction

The increase in biofuel production by 28 % from 2021 to 2026 [1] would lead to the excessive amount of glycerol and impact the sustainability of biodiesel industry [2]. Hence, the utilization of glycerol by any mean is needed to overcome this problem. Glycerol is listed as one of the top twelve building block chemicals, owing to its functionality as a raw material to produce higher valuable chemicals, such as 1,2-propanediol, lactic acid, acrolein, acrylic acid, and polymers [3]. Lactic acid is a prominent platform chemical, whose production relies on fermentation process operated commercially with several disadvantages, such as low productivity and an additional expenses for isolation and purification of the products [4]. Thus, an alternative production route is extensively studied by a large number of researchers to achieve more highly economical production.

As one of the alternative to achieve more economical and faster lactic acid production, the catalytic conversion of glycerol to lactic acid can be divided into two groups; that are, selective oxidation and hydrothermal reactions [5]. The selective oxidation is usually

* Corresponding author.
E-mail address: sirirat.j@chula.ac.th (S. Jitkarnka).

https://doi.org/10.1016/j.heliyon.2024.e30325
Received 20 December 2023; Received in revised form 23 March 2024; Accepted 23 April 2024
Available online 28 April 2024

conducted in the presence of an oxidant, i.e., O_2 and in a mild condition at a temperature of 90–100 °C [6], forming other oxygenated products, such as glyceric acid and pyruvic acid as a by-product [7,8]. On the other hand, the hydrothermal reaction is usually conducted at a higher temperature at 180–290 °C with the co-production of 1,2-propanediol as a side product during the reaction. Furthermore, the reaction is usually conducted with the presence of an alkaline such as NaOH [9,10] and $Ca(OH)_2$ [11], using either homogeneous catalysts such as Mn-complexes [12] or heterogeneous catalysts, like Pd/hydroxyapatite [10], Cu/hydroxyapatite [13], CuPdx [9], Pt [14], and Co_3O_4/CeO_2 catalysts [15] in order to enhance the selectivity and yield of lactic acid, which is one of the hurdles for commercialization due to the harsh condition and an additional treatment cost as a result of the formation of lactate salts at the end of the reaction [12]. Thus, a base-free condition is more favored.

Scheme 1 summarizes the reported pathways for the glycerol conversion to lactic acid. The first pathway initially involves with the dehydration of glycerol via Lewis acid sites to form acetol [16]. Then, the subsequent reactions are divided into two routes; that are, (i) the first one involves with the hydrogenation of acetol via metal sites [17,18] to 1,2-propanediol that is oxidized to form lactaldehyde [19], and lactaldehyde is further converted to lactic acid in an oxidizing condition [19], and (ii) the second one involves with the oxidation of acetol to pyruvaldehyde [16] that subsequently undergoes the Cannizzaro reaction to lactic acid in the presence of a homogeneous- or an aqueous base [15,21] as well as a Lewis acid site of a catalyst [20,22]. Concurrently, the second pathway involves with the dehydrogenation of glycerol to glyceraldehyde over a heterogeneous base catalyst [13–15], giving off H_2 that can be supplied to the acetol hydrogenation step, followed by the dehydration of glyceraldehyde and then the keto-enol transformation of glyceraldehyde to pyruvaldehyde [13–15]. After that, the Cannizzaro reaction takes place under a basic condition to produce lactic acid [15,21]. Among the three routes, the dehydration-oxidation pathway of glycerol is the most prospect way to produce lactic acid because it is much shorter, and advantageously can be conducted in a homogeneous base-free condition. Inevitably, 1,2-propanediol can be concurrently formed via acetol hydrogenation in the first route as well. Namely, after the dehydration of glycerol, acetol formed as the product can also undergo the hydrogenation reaction on a metal site, which finally produces 1,2-propanediol [17,18]. As a result, the dehydration-oxidation pathway is possibly one of the prospect alternative and sustainable ways to simultaneously produce lactic acid and 1,2-propanediol.

According to Scheme 1, one of the important intermediates is acetol that can be formed via the dehydration of glycerol, and acid and basic sites of catalysts were reported to govern the selectivity of acetol. Among various Mg supports; namely, MgO, MgF(OH), and MgF_2, the highest acetol yield was obtained with using MgF_2 support, which was found to have the highest Lewis acid sites, suggesting the formation of acetol was driven by the Lewis acid sites of the catalysts [23–25]. However, to further convert acetol to the 1,2-propanediol, a metal site was required [18,26]. Thus, a catalyst that has acid and metal sites are needed to form both 1,2-propanediol and then lactic acid. Nowadays, layered double hydroxide (LDH) materials have received high attention on glycerol conversion. The advantages are on the acid-basic pairs that can be adjusted by changing the M^{2+}/M^{3+} molar ratio, and also on other metals that can also be incorporated in the structure, which could enhance the properties of the materials [27]. The dehydration of glycerol to acetol has been studied using the materials as the catalysts at different calcination temperatures [28]. It was found that the corresponding Layered Double Oxides (LDOs), formed after calcining the LDH materials, enhanced acetol yield when employed as catalysts for glycerol conversion. The optimum calcination temperature to achieve the highest yield of acetol was found to be 500 °C, and above 500 °C the formation of by-products was observed. Without the addition of an alkaline, Cu-LDO catalysts have also recently been employed for glycerol conversion [27]. The incorporation of Cu into the MgAl-LDO sheets resulted in the increases of glycerol conversion and acetol yield. The resulting and previously-existing Cu^{2+} and Cu^{+} were proven to be the active species a high selectivity towards acetol. Moreover, it was found that the catalysts were reduced during the course of acetol dehydration, and Cu^0 species was highly selective to 1,2-propanediol. However, the formation of 1,2-propanediol via glycerol hydrogenolysis requires H_2 supply because it involves with C–C or C-heteroatom bond scission that is usually carried out at high temperature and pressure conditions [18,26]; hence, the needs of H_2 external gas and the harsh operating conditions are the main drawbacks. A thrifty way to form 1,2-propanediol

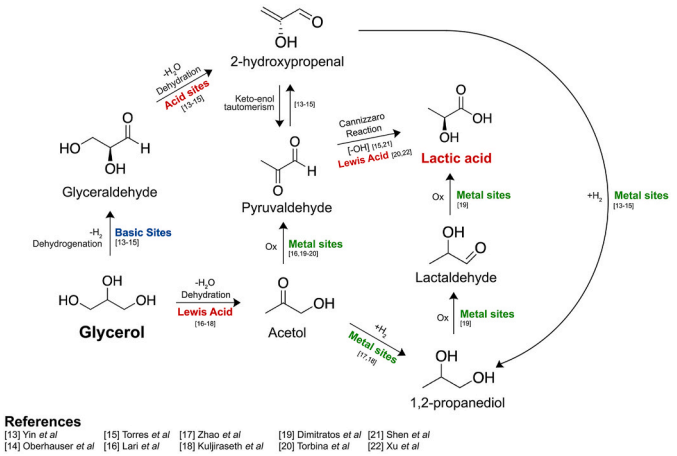

Scheme 1. Possible pathways of glycerol conversion to lactic acid as collected from literatures.

is to conduct under external H_2-free condition at the situations where H_2 can be possibly generated *in-situ* from several co-driven reactions, such as the dehydrogenation of glycerol to glyceraldehyde and glycerol reforming, using some selective catalysts [29], or by the addition of a hydrogen donor [30]. For instance, a $Cu_{0.3}Mg_{3.7}AlO$ LDO was employed as a catalyst for the conversion of glycerol, and found to give 34.9 % selectivity towards 1,2-propanediol in an external H_2-free condition [18]. Moreover, further addition of ethanol as a hydrogen donor was proven to form *in-situ* H_2; however, it resulted in the decrease in 1,2-propanediol selectivity because 1,2-propanediol was further oxidized into ethyl lactate [18].

Normally, the use of a homogeneous base is essential for a high lactic acid yield. For instance, the glycerol conversion to lactic acid has been previously studied in two environments; that are, either neutral or basic [31]. In neutral environment, the formation of 1, 2-propanediol was more favored, while in the basic one, the selectivity towards lactic acid was greatly enhanced. Therefore, the presence of a base is essential for the lactic acid formation; however, its uses consequently result in some additional separation and purification costs due to the formation of lactate salts. Hence, a base-free condition is more preferred. The synthesis of lactic acid from glycerol in a base-free condition using bifunctional Pt/Sn-MFI catalysts has been reported to achieve 80.5 % selectivity [32]. The presence of Pt provided the metal sites that drove the selective oxidation of glycerol to glyceraldehyde, whereas Sn-MFI with a high amount of Lewis acid sites as active sites led to the high formation of lactic acid [32]. A similar finding was also obtained using Ag_3PMo as a catalyst with the presence of Ag (I) oxide that was found to enhance the activity of glycerol oxidation [33]. Moreover, the high yield of lactic acid was also achieved, which was attributed to the high amount of strong Lewis acid sites. Accordingly, to achieve a high yield of lactic acid from glycerol conversion under a base-free condition, a multi-functional catalyst that contains acid and metal sites is required. A core-shell catalyst can be one of the possible alternatives, due to its ability to combine the desired properties of each materials component [34]. The uses of core-shell catalysts on glycerol conversion have been studied. For examples, an investigation of different catalytic structure was done on the conversion of glycerol to 1,2-propanediol with an addition of external H_2 gas. The $Cu_{1.1}$/ZnO core-shell catalyst exhibited the prominent activity with 85.7 % conversion and 82.3 % 1,2-propanediol selectivity than the catalysts with other structures. The partial embedment by ZnO was found to enhance the adsorption and activation of H_2, which improved the catalytic activity. Furthermore, it prevented Cu from sintering, and then maintained the stability [35]. Moreover, the activity on glycerol conversion to lactic acid and reusability of a shell@core Ni-NiO_x@C catalyst were compared to those of the other supported Ni- and Ni-NiO_x/C catalysts with the presence of a base [36]. The core-shell structured Ni catalyst was found to have the highest catalytic performance with 46.8 % yield of lactic acid as a result of the properly-grown amount of NiO_x and metallic Ni that led to the superior catalytic performances, whereas the supported Ni catalyst produced only 10.6 % lactic acid yield. Moreover, in the core-shell structure, the full coverage of carbon also provided some protection to Ni, and prevented it from leaching and over-oxidation, finally resulting in a better catalyst stability [36]. In summary, a core-shell catalyst structure has a better catalytic activity due to the unique interaction between the outer and inner materials, and provides a better stability than the conventional supported catalysts. Nevertheless, the use of core-shell structured catalysts in the absence of a base and external H_2 gas has rarely been found in published articles nowadays.

In our preliminary work, Ag/Sn-zeolite catalysts have been investigated for the conversion of acetol to valuable chemicals [37,38]. The catalysts were found to mainly govern the oxidation reaction, giving off 40 % oxidation products. Nevertheless, it was able to simultaneously produce both 1,2-propanediol and lactic acid with a low selectivity. From the literature review, it is evident that the conversion of glycerol for producing lactic acid and 1,2-propanediol under a base-free and external H_2-free condition requires (a) Lewis acid sites, expected to drive the glycerol dehydration and Cannizzaro reaction, and (b) metallic sites playing the roles on the acetol hydrogenation and all oxidation reactions. In addition, a core-shell structure has been proven to be essential to support such complex reactions [35,36,39]. Consequently, the purposes of this study were to investigate the influences of core-shell catalysts, consisting of Ag@Sn/ZSM-5 as the core and $Ni_xMg_{4-x}AlO$ with various Ni: Mg ratios as the catalyst shell, for the production of lactic acid from glycerol under a homogeneous base-free and external H_2-free condition. Owing to the acid-base pairs on $Ni_xMg_{4-x}AlO$, the Lewis acid sites were expected to enhance the dehydration of glycerol, leading to the formation of acetol, while the base sites were supposed to drive the *in-situ* hydrogen formation to supply to the acetol hydrogenation step so that the system can be operated under an external H_2-free condition. The ratio of Ni: Mg was consequently varied in order to determine the optimum ratio that led to the highest catalytic activity. Subsequently, the Ag@Sn/ZSM-5 was expected to sequentially drive the oxidation of acetol to pyruvaldehyde, whereas the Sn/ZSM-5 was then anticipated in driving the transformation of pyruvaldehyde to lactic acid under a base-free condition.

2. Experimentals

2.1. Catalyst preparation

At the beginning, AgO@SnO_2/ZSM-5 was synthesized using the previously-reported method [37]. Namely, a ZSM-5 zeolite (Si/Al: 15 from Zeolyst International) was pretreated by calcination at 550 °C for 6 h, resulting in the formation of H^+-ZSM-5. Next, 33 mL of 1 M $SnCl_2 \cdot 2H_2O$ solution was added to 2 g of H^+-ZSM-5 under continuous stirring. The mixture was then stirred at room temperature for 24 h, and after that the solid was separated by centrifugation, washed, and dried in the oven for overnight to obtain SnO_2/ZSM-5.

Next, AgO@SnO_2/ZSM-5 was prepared first by loading 20%wt of Ag (1.4 g of $AgNO_3$ in 15 mL DI water) into 3 g of SnO_2/ZSM-5 under continuous stirring for 18 h. The solid was then separated from the mixture by centrifuge, washed with deionized water, and then dried in the oven for overnight. The AgO@SnO_2/ZSM-5 was obtained after calcination at 500 °C for 6 h.

The $Ni_xMg_{4-x}AlO$-embedded AgO@SnO_2/ZSM-5 catalysts were synthesized by co-precipitation method. **Mixture A** was prepared by adding 2 g of AgO/SnO_2@ZSM-5 in 40 mL deionized water, followed by sonication for 30 min and the addition of 2 g Na_2CO_3 with subsequent sonication for another 6 min. Later, **Mixture B** was prepared with the amount of $Al(NO_3)_3 \cdot 9H_2O$ fixed at 3.75 g, 9.74 g of

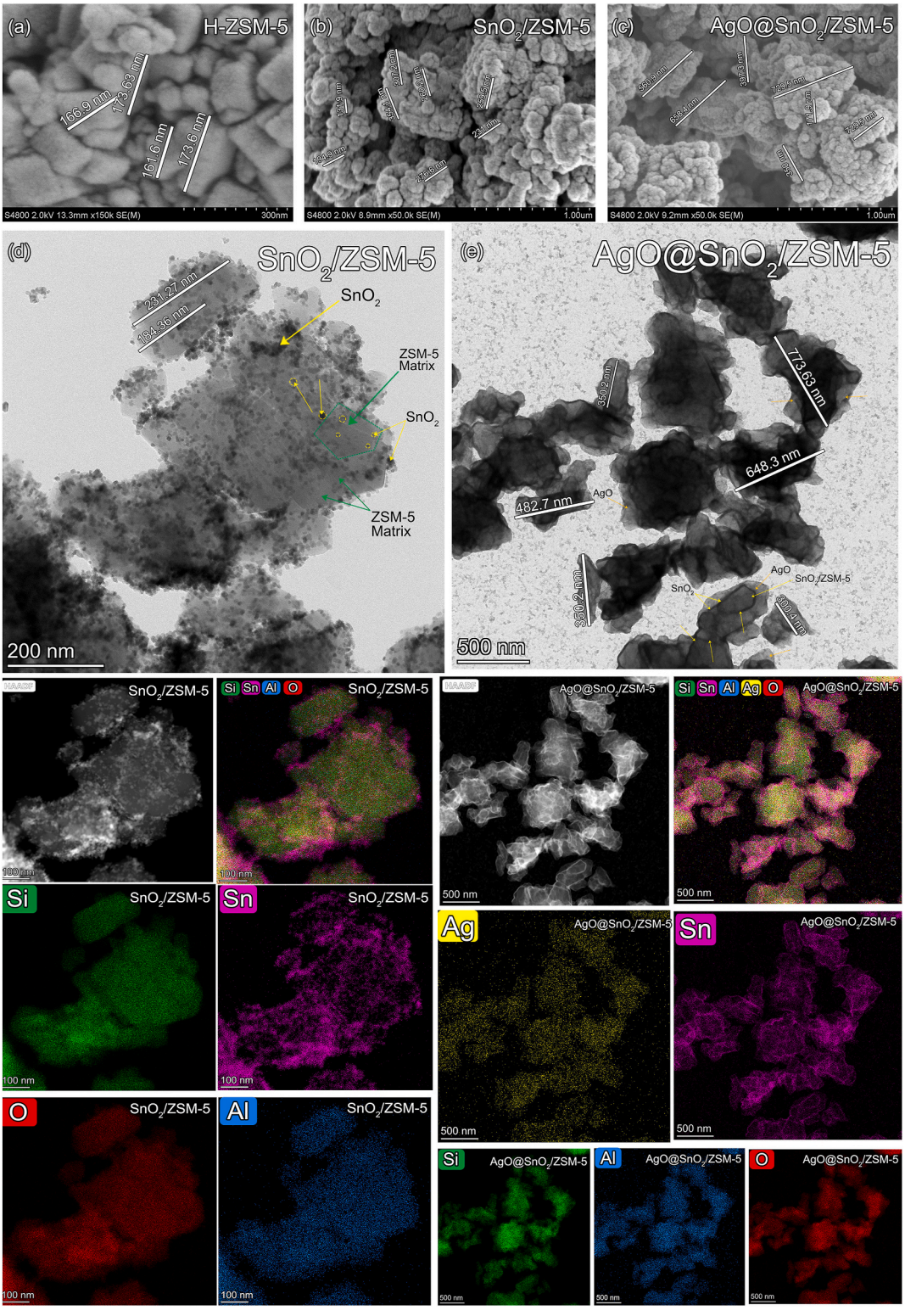

Fig. 1. FE-SEM Images of (a) H-ZSM-5, (b) SnO_2/ZSM-5, and (c) AgO@ SnO_2/ZSM-5, and HR-TEM images and EDX mapping of (d) SnO_2/ZSM-5, (e) AgO@SnO_2/ZSM-5.

$Mg(NO_3)_2 \cdot 6H_2O$ and 0.58 g of $Ni(NO_3)_2 \cdot 6H_2O$. Then, **Mixture B** was added into **Mixture A** with the pump rates of 45 mL/min under vigorous stirring with the pH of the solution was maintained at 10 by adding 4 M of NaOH. After 1 h of stirring, the mixture was then centrifuged. Next, the obtained precipitate was added into 40 mL deionized water, followed by stirring for another hour. Subsequently, the slurry was centrifuged, and the solid precipitate was washed using deionized water until the pH reached 7. Finally, the obtained shell@core catalysts with Ni/Mg ratio of 0.2/3.8 were dried in the oven for overnight, followed by calcination for 5 h at 500 °C. The catalysts with the other Ni/Mg ratios of 0.3/3.7, 0.4/3.6, and 0.5/3.5 were also prepared using the same procedure.

2.2. Catalyst characterization

X-Ray powder diffraction (XRD) was employed to determine the crystallinity of catalyst samples and the morphology of catalysts. The XRD patterns were recorded using Rigaku SmartLab X-Ray Diffractometer in the range of 5-80° with the scan of 0.02° (2θ) steps/0.6 s. X-ray fluorescence spectrometer (XRF) was performed to determine the elemental concentration of the catalyst samples using Bruker S8 Tiger WDXRF spectrometer. Surface area analyzer (Quantachrome, QS-evo MP) was employed to determine the specific surface are, pore size, and total pore volume of the catalyst. The surface and morphology of the catalysts were observed by using a Field Emission Scanning Electron Microscopy (FE-SEM), Hitachi/S-4800. Transmission electron microscopy (TEM) was performed using a Thermo Scientific TALOS F200X (FE-TEM), and the elemental mapping was conducted using an EDX detector. X-Ray Photoelectron spectroscopy (XPS) was carried using the AXIS ULTRA^{DLD} to determine the oxidation state and chemical bonding of elements in the samples.

The temperature programmed desorption of ammonia (NH_3-TPD) and carbon dioxide (CO_2-TPD) were employed to determine the acidity and basicity of the catalysts using TPDRO Analyzer, BELCAT II. The catalysts were pretreated in He gas at 450 °C for 60 min, and then pre-adsorbed the 10 % NH_3/He or 99.9995 % CO_2 at 100 °C for 30 min. After that, temperature was increased to 650 °C at 10 °C min^{-1} and held for 30 min with He. X-ray absorption near edge structure (XANES) and extended x-ray absorption fine structure (EXAFS), were performed in the transmission mode at room temperature for the Ni K-edges in order to investigate the structure of catalyst shells at different Ni/Mg ratios at Beamline 8 of the Synchrotron Light Research Institute (SLRI), Thailand [40]. The XANES and EXAFS data were then processed using the ATHENA and ARTEMIS softwares [41]. The catalyst composition was determined using linear combination fitting (LCF), while the coordination number and type of neighboring atoms were identified by the ARTEMIS program.

2.3. Activity testing

The catalytic conversion of glycerol was performed using a PARR reactor. A 40 mL of glycerol (99.5 % AR Grade, QRëc) and 1 g of a catalyst were added into the reactor, and the air inside was removed by purging the reactor with N_2 gas for 30 min. The reaction was then conducted at 180 °C for 4 h under 300 rpm stirring rate without the addition of an alkali solution or external H_2 gas. After 4 h of residence time, the reactor was then cooled down to room temperature, and the liquid product was separated from the catalyst by centrifugation, and later analyzed using a 1D-Mode Pegasus LECO GC-TOF/MS. The conversion and product selectivity were calculated using the following equations:

$$\text{Glycerol Conversion } (\%) = \frac{Concentration\ of\ Gly_{in} - Concentration\ of\ Gly_{out}}{Concentration\ of\ Gly_{in}} \times 100$$

$$\text{Selectivity of Product } i\ (\%) = \frac{Concentration_i\ (wt\%)}{\sum_{i=o}^{n} Concentration_i\ (wt\%)} \times 100$$

$$\text{Yield of Product } i\ (\%) = \frac{Selectivity_i(\%) \times \text{Glycerol Conversion } (\%)}{100}$$

It is hereby noted that since the required Lewis acid sites, formed only after the LDHs are calcined to the corresponding LDOs, were expected to drive the glycerol dehydration as well as the Cannizzaro reaction, only the LDO form of the composite materials was therefore tested for the activity. Moreover, the LDH form is not usually stable in the reaction condition conducted at 180 °C for 4 h under 300 rpm stirring rate, even without an alkaline addition. Hence, the activity testing was only performed on the LDO-embedded samples in this work. However, the LDH form of samples was also prepared as the references in order to investigate the change in the local environment and ensure the phase transformation of the LDOs before (LDHs) and after calcination (LDOs).

3. Results and discussion

3.1. Determination of catalyst formation

To elucidate the morphology and structure of the catalysts, the FE-SEM and TEM-EDX techniques were first employed, and the results are presented at every steps of preparation in Fig. 1. The FE-SEM images in Fig. 1(a) show that the commercial H-ZSM-5 clearly has an uneven cuboid structure with the average size of ~160 nm, and then the sample size in Fig. 1(b–c) at each preparation step increases from ~160 nm (H-ZSM-5) to ~200–300 nm (SnO_2/ZSM-5 agglomerates) and to ~550–750 nm (AgO@SnO_2/ZSM-5

agglomerates), indicating the sequential coverages of SnO_2 and then AgO onto H-ZSM-5. Moreover, the TEM image in Fig. 1(d) and elemental mapping also depict that SnO_2 is mostly crowded between grains of the zeolite, resulting in the bigger agglomerates with an average size of ~260 nm. Subsequently, after the further deposition of AgO onto SnO_2/ZSM-5, SnO_2/ZSM-5 is fully covered by AgO as depicted in Fig. 1(c). Apparently, the elemental mapping (Fig. 1(e)) also exhibits and confirms that a shell of Ag species is formed and fully cover the clusters of SnO_2/ZSM-5. Furthermore, the XRD pattern in Fig. 2 exhibits the diffraction peaks of SnO_2 at 26.7°, 33.9°, 51.9°, and 58.2° [42] and of AgO at 33° and 57.43° [42,43]. At this stage, a sandwiched core-shell catalyst [34] is formed as illustrated in Fig. 3 that apparently illustrates the complete coverage of AgO shell around the SnO_2/ZSM-5 core. Thus, the sandwiched core-shell catalyst at this step is denoted as "**AgO@SnO_2/ZSM-5**", where AgO is the shell, and SnO_2/ZSM-5 is the core.

In the next step of preparation, a $Ni_xMg_{4-x}AlO$ was grown on the AgO@SnO_2/ZSM-5 powder, and the XRD was performed on the resulting materials, as the patterns are shown in Fig. 2. The XRD patterns of the LDH samples, shown in Fig. 2(a) as references, indicate the characteristics of hydrotalcite phase at 2θ of 11.19°, 22.69°, 38.49°, 45.6°, 61.55°, which correspond to (003), (006), (015), (018), and (113) planes [18,44]. Fig. 2(b) exhibits that after calcination at 500 °C, the hydrotalcite phase disappears with the formation of MgO (periclase), NiO (bunsenite) at 43.5° and 62.9°, and 75.4° are detected [45,46], which implies the collapse of LDH interlayer after calcination [47], forming LDOs as confirmed by the characteristics diffraction peaks of $MgAl_2O_4$ spinel at 44.86° detected in all $Ni_xMg_{4-x}AlO$ samples [48]. As supported by the SEM and TEM images, Fig. 4(a–d) shows the agglomeration of $Ni_xMg_{4-x}AlO$, identified by the formation of uneven rectangular sheets covering the AgO@SnO_2/ZSM-5 clusters. The formation of catalysts at this stage is generally matched with an embedded core-shell type defined by Das et al. (2020) [34], and the catalysts then called the "**Ni_xMg_{4-x}AlO-embedded AgO@SnO_2/ZSM-5**" as depicted in Fig. 5(a). They consist of $Ni_xMg_{4-x}AlO$ lodges that embed the sandwiched core-shell type AgO@SnO_2/ZSM-5 cluster.

In addition, the elemental mapping in Fig. S1(a) of supplementary documents reveals that the ratio of Ni affects the formation of $Ni_xMg_{4-x}AlO$ lodges around the AgO@SnO_2/ZSM-5 clusters. At the lowest Ni ratio of 0.2, the $Ni_xMg_{4-x}AlO$ layer seems to partially cover the AgO@SnO_2/ZSM-5 clusters, as depicted in Fig. 5(a). As a result, a sandwiched core-shell catalyst of the embedded type is formed [34,49]. With the increasing Ni ratio, $Ni_xMg_{4-x}AlO$ starts to cover the clusters more and more. Finally, at the highest Ni/Mg ratio of 0.5/3.5, the shell of $Ni_xMg_{4-x}AlO$ is formed, fully covering the AgO@SnO_2/ZSM-5 clusters, indicating the embedment of AgO@SnO_2/ZSM-5 in the bulk of $Ni_xMg_{4-x}AlO$. At this stage, a completely-embedded sandwiched core-shell type catalyst is formed [34,49] as illustrated in Fig. 5(b). In summary, it can be concluded that (1) when the Ni/Mg ratio is below or equal to 0.3/3.7, the catalysts can be categorized as a sandwiched core-shell catalyst of the embedded type, and (2) when the Ni/Mg ratio is higher or equal to 0.4/3.6, they turn into a completely-embedded sandwiched core-shell type, as illustrated in Fig. 5.

Additionally, the embedding $Ni_xMg_{4-x}AlO$ lodges were investigated for the local environments at various Ni/Mg ratios using XRD, XPS, XANES, and EXAFS. In order to investigate the phase transformation, the structures before (LDHs) and after calcination (LDOs) were compared. The Mg 2p XPS spectra of the materials before (LDHs) and after calcination (LDOs) are presented in Fig. 6. In the LDH form, the Mg 2p deconvolution exhibits two peaks that correspond to the Mg–OH (48.3 eV) and Mg–CO_3 (49.7 eV) binding energies. After calcination, the shifts of Mg 2p peaks towards a higher binding energy are observed on all samples, indicating a change in local environment on the embedding LDH lodges, which was previously found also in the XRD results. Furthermore, the deconvolution of Mg 2p XPS spectra on the LDO lodges exhibits three peaks that correspond to the Mg–O, Mg–*O*–Al, and Mg–OH binding energies [45]. In addition, with the increasing ratio of Ni from 0.2 to 0.5, the Mg 2p peaks of LDO shift to a higher binding energy towards the Mg–*O*–Al and Mg–O phases, implying that at a higher Ni ratio, the Mg sites were not further replaced by the Ni^{2+} species. Fig. 6 (b) displays the Ni 2p XPS spectra, contributed from spin-orbit doublets (Ni $2p_{3/2}$ and $2p_{1/2}$) and satellites (labeled as "sat") of both LDH- and LDO-embedded samples. For the LDH-embedded samples, the deconvolution peaks display two peaks at binding energies of 853.8 eV and 854.9 eV, which correspond to Ni^{2+}-O and Ni^{2+}-OH bonding. Apparently, the addition of Ni does not seem to make any changes in the local environment of LDH lodges since no peak shifts are noted when the Ni ratio increases from 0.2 to 0.5. In contrast, for the

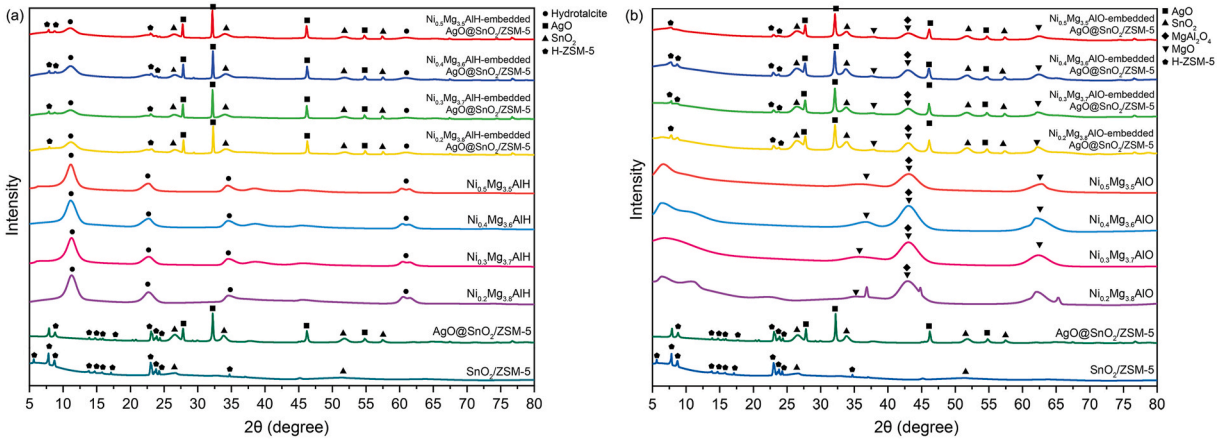

Fig. 2. XRD patterns of (a) Ni_xMg_{4-x}AlH-embedded AgO@SnO_2/ZSM-5 and (b) $Ni_xMg_{4-x}AlO$-embedded AgO@SnO_2/ZSM-5 catalysts in comparison with those of all the components.

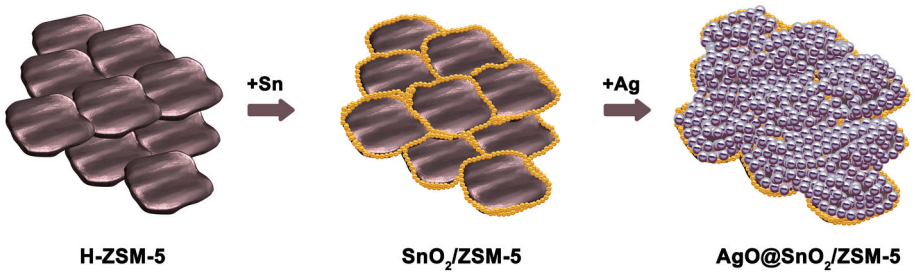

Fig. 3. Illustration of the formation of SnO_2/ZSM-5 and AgO@SnO_2/ZSM-5 catalysts.

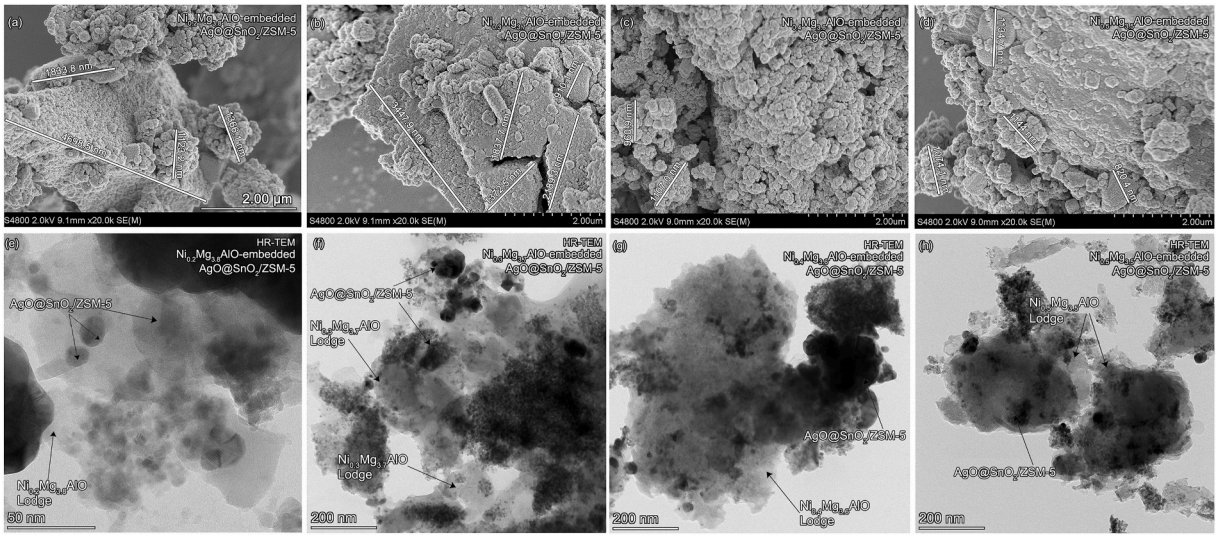

Fig. 4. HR-TEM images and FE-SEM images of (a) $Ni_{0.2}Mg_{3.8}AlO$-embedded AgO@SnO_2/ZSM-5, (b) $Ni_{0.3}Mg_{3.7}AlO$-embedded AgO@SnO_2/ZSM-5, (c) $Ni_{0.4}Mg_{3.6}AlO$-embedded AgO@SnO_2/ZSM-5, and (d) $Ni_{0.5}Mg_{3.5}AlO$-embedded AgO@SnO_2/ZSM-5 catalysts.

LDO-embedded samples, the significant chemical shifts in the Ni 2p spectra are observed. The Ni $2p_{3/2}$ peaks observed from NiO standard is located ~853.8 eV and ~855.5 eV. At the Ni ratio of 0.2, the peaks shift toward higher binding energies of ~857 eV, assigned to the $Ni^{\delta+}$-O ($2< \delta < 3$), and ~858.6 eV, assigned to the octahedral Ni^{2+} in $NiAl_2O_4$ [50], likely because some Ni^{2+} may attempt to locally replace the Mg^{2+} sites, next to Al^{3+} sites, inside the LDO structure. At the Ni ratio of 0.3, the peaks shift further towards a higher binding energy, indicating that more Ni^{2+} substitutes the Mg–*O*–Al sites, forming Ni–*O*–Al bond. From the ratios of 0.3–0.5, the shifts move back a lower binding energy, suggesting the saturation of the Ni substitution and then resulting in the formation of NiO clusters outside the LDO structure. In addition, the formation of $Ni^{\delta+}$ species is further confirmed by the O_{1s} XPS results in Fig. 6(c), which reveal two deconvoluted peaks attributed to chemisorbed oxygen (O_α) at a lower B.E. and lattice oxygen (O_β) at a higher B.E [51]. At lower Ni ratio $\leq$0.3, a larger value of $O_\alpha/(O_\alpha+O_\beta)$ ratio (Table 1) implies that the catalysts exhibit a lower electron density around the surface oxygen species than the ones at Ni ratio $\geq$0.4, which causes a negative charge transfer from the Ni sites, then forming Ni species with higher oxidation states than +2 [51]. These observations are further confirmed and elucidated by the XANES results.

The analysis details of Ni K-Edge XANES spectra of $Ni_xMg_{4-x}AlH$ and $Ni_xMg_{4-x}AlO$ on AgO@SnO_2/ZSM-5 catalysts are provided in Fig. S2 ofthe supplementary documents. In summary, the LDH samples was found to adopt the symmetric octahedral geometries evinced by the presence of weak absorption pre-edge at ~8332.8 eV [52,53]. After calcination, there was a slight change in the local environment of Ni, which can be seen from the formation of shoulder peaks at ~8342 eV that suggests the presence of another coordinating sites outside the octahedral geometries [42,54]. Moreover, a similar fashion as in the XPS spectra is also observed from the phase compositions calculated using the Linear Combination Fitting (LCF) tool in ATHENA by fitting the Ni K-Edge spectra with its Ni standards. The fitting results are provided in Table 1. In the LDH form, Ni elements are mostly in the Ni^{2+}-O species, while after calcination, the Ni elements at the ratios of 0.2 and 0.3 are in the forms of Ni^{2+}-O and Ni^{4+}-O species (with the average Ni oxidation states of 2.4–2.5), and at the higher ratios of Ni (0.4 and 0.5) only the formation of Ni^{2+}-O species exists.

Subsequently, the local environment around atoms of the $Ni_xMg_{4-x}AlO$ lodges was further analyzed using EXAFS, and the fitting details are provided in Fig. S3 of the supplementary document. Both LDH and LDO samples provide two main peaks; that are, the first peak centered at ~1.6 Å that is contributed from the Ni–O scattering path, and the second peak centered around ~2.5 Å are attributed

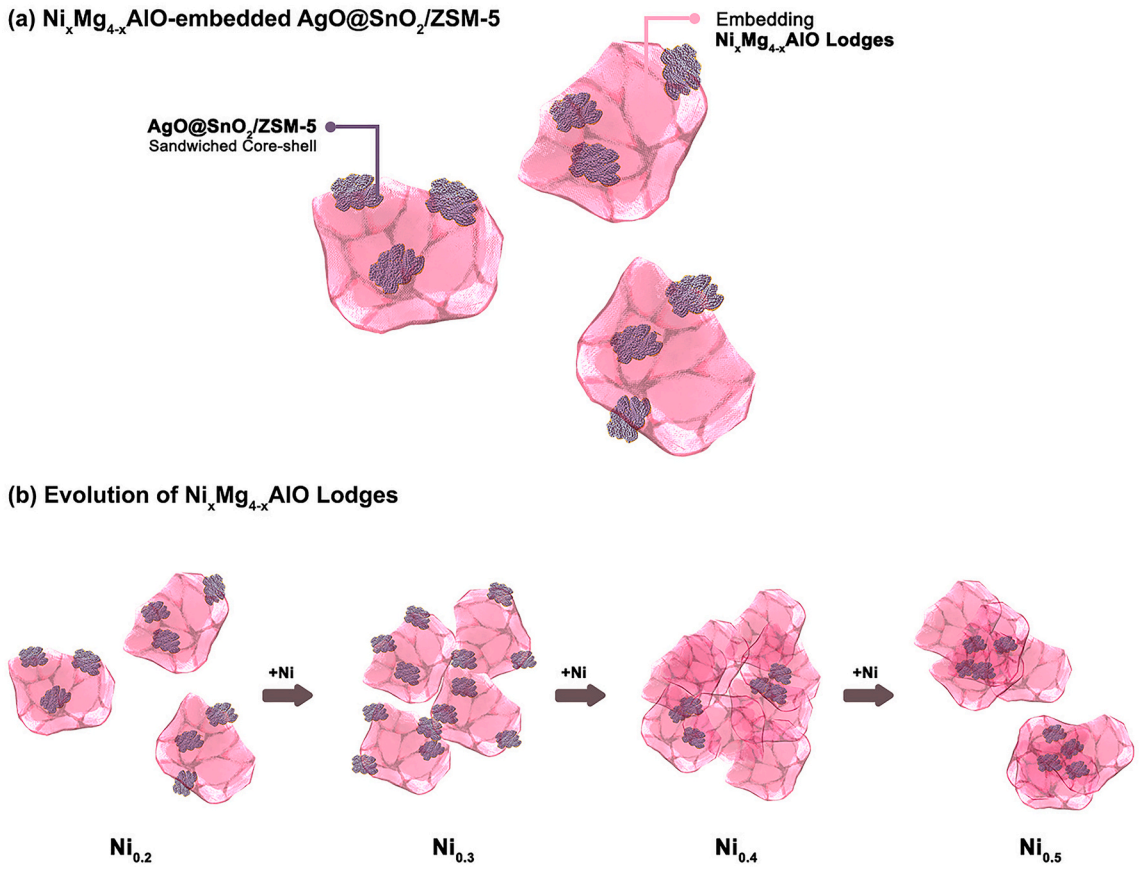

Fig. 5. (a) Illustration of $Ni_xMg_{4-x}AlO$-embedded $AgO@SnO_2/ZSM-5$ and (b) the evolution of $Ni_xMg_{4-x}AlO$ lodges.

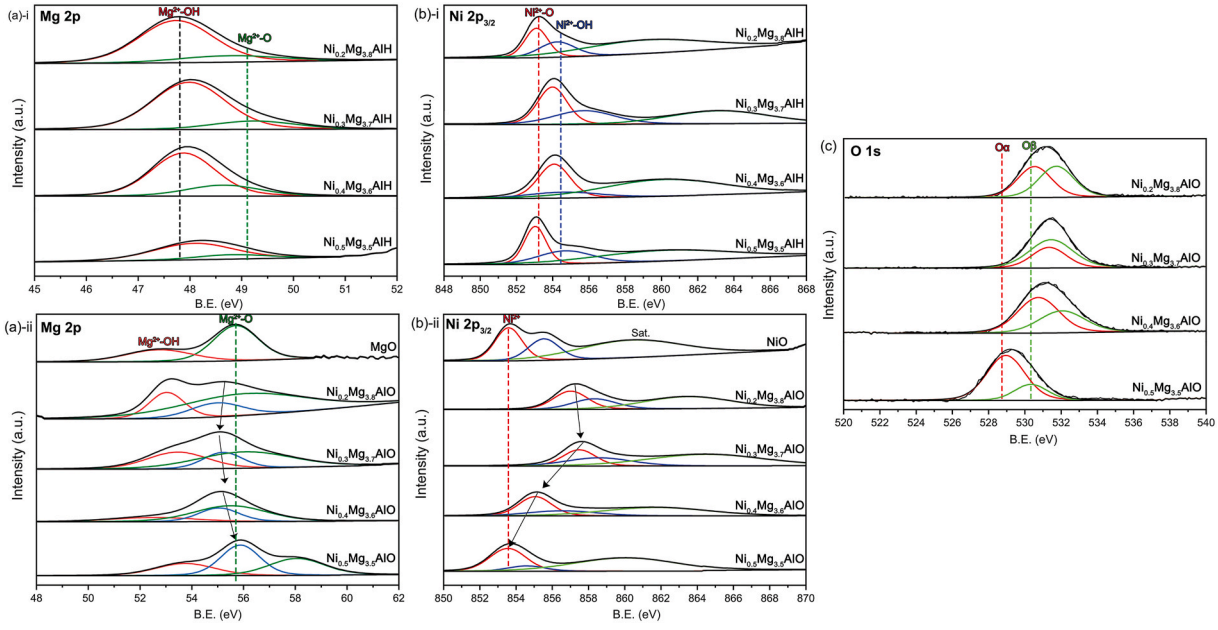

Fig. 6. XPS spectra: (a) Mg_{2p}, (b) Ni_{2p}, and (c) O_{1S} of $Ni_xMg_{4-x}AlH$ and $Ni_xMg_{4-x}AlO$.

Table 1
Phase compositions in the $Ni_xMg_{4-x}AlO$-embedded $AgO@SnO_2$/ZSM-5 catalysts before and after calcination from Linear Combination Fitting.

Sample			Ratio of $O_\alpha/(O_\alpha+O_\beta)$	Ni K-edge			Ni Oxidation state[a]	R Factor
Form	Name	Extent of embedment		% Composition				
				NiO	NiO_2	Ni Foil		
$Ni_xMg_{4-x}AlH$ on $AgO@SnO_2$/ZSM-5								
LDH	$Ni_{0.2}Mg_{3.8}AlH$	Partial	–	94.7	5.3	0	2.0	0.0205
	$Ni_{0.3}Mg_{3.7}AlH$	Partial	–	95.2	4.8	0	2.0	0.0197
	$Ni_{0.4}Mg_{3.6}AlH$	Complete	–	100	0	0	2.0	0.0144
	$Ni_{0.5}Mg_{3.5}AlH$	Complete	–	100	0	0	2.0	0.0227
$Ni_xMg_{4-x}AlO$ on $AgO@SnO_2$/ZSM-5								
LDO	$Ni_{0.2}Mg_{3.8}AlO$	Partial	0.51	66.3	33.4	0	2.4	0.0185
	$Ni_{0.3}Mg_{3.7}AlO$	Partial	0.63	83.6	16.4	0	2.5	0.0147
	$Ni_{0.4}Mg_{3.6}AlO$	Complete	0.41	100	0	0	2.1	0.0166
	$Ni_{0.5}Mg_{3.5}AlO$	Complete	0.24	100	0	0	2.0	0.0165

[a] Calculated from Ni K-edge of the Ni references employed in the XANES experiments.

to the Ni–Mg and Ni–Al scattering path. Similar to their Ni K-Edge XANES spectra, the change in the local environment of Ni after calcination is also observed from the EXAFS. Previously, the presence of shoulder peaks that signify the hydroxide bonded with Ni the LDH samples are present around ~1.1 Å and ~2.2. After calcination, these two shoulder peaks disappear, indicating that the hydroxide previously bonded with Ni has changed its form after calcination. Moreover, the calcination also appears to affect the bond distances and coordination number of Ni–Mg bond (Table 2). A decrease in Ni–O coordination number, along with the increase of coordination number of Ni–Mg from ~6 to ~12, suggesting a change in geometric structure after calcination [53,54]. According to the EXAFS results, it shows that in calcined formed, the $Ni_xMg_{4-x}AlO$ lodges where consists of MgO and $MgAl_2O_4$ structures with no other structure exists, which also confirmed by the previous XRD results. The fitting shows that the Ni^{2+} ions replace the Mg sites of the MgO structure inside Mg_4AlO lodges, and locally some of the Ni^{2+} ions also able to replace the Al sites inside the $MgAl_2O_4$ structure. Moreover, the effect of increasing Ni ratio can be observed on the radius of Ni–*O*–Mg bond on the LDO lodges. There are no any significant changes in both bond length and the coordination number on Ni–O and Ni–*O*-M bonds (M = Mg or Al) with increasing

Table 2
Structural parameters from the Ni–K Edge EXAFS spectra for $Ni_xMg_{4-x}AlO$ embedded- $AgO@SnO_2$/ZSM-5 catalysts.

Sample		Ni K-Edge				
Form	Name	Bond Type	C·N.	R (Å)	ss	R factor
$Ni_xMg_{4-x}AlH$ on $AgO@SnO_2$/ZSM-5						
LDH	**$Ni_{0.2}Mg_{3.8}AlH$**	Ni–O	6.5 ± (0.5)	2.03 ± (0.008)	0.007	0.015
		Ni–*O*–Mg	6.4 ± (0.46)	3.01 ± (0.008)	0.008	
		Ni–*O*–Al	7.0 ± (5.1)	2.64 ± (0.050)	0.00001	
	$Ni_{0.3}Mg_{3.7}AlH$	Ni–O	6.4 ± (0.6)	2.07 ± (0.004)	0.001	0.013
		Ni–*O*–Mg	6.2 ± (1.1)	2.86 ± (0.008)	0.004	
		Ni–*O*–Al	7.5 ± (3.6)	2.83± (0.033)	0.013	
	$Ni_{0.4}Mg_{3.8}AlH$	Ni–O	6.1± (0.6)	2.08 ± (0.005)	0.004	0.011
		Ni–*O*–Mg	6.1 ± (0.5)	2.86 ± (0.009)	0.005	
		Ni–*O*–Al	7.4 ± (6.3)	2.77 ± (0.034)	0.031	
	$Ni_{0.5}Mg_{3.5}AlH$	Ni–O	6.4 ± (0.4)	2.06 ± (0.004)	0.004	0.008
		Ni–*O*–Mg	6.1 ± (0.5)	2.86 ± (0.009)	0.006	
		Ni–*O*–Al	7.5 ± (3.4)	2.80 ± (0.059)	0.012	
$Ni_xMg_{4-x}AlO$ on $AgO@SnO_2$/ZSM-5						
LDO	**$Ni_{0.2}Mg_{3.8}AlO$**	Ni–O	6.1 ± (0.3)	2.08 ± (0.008)	0.008	0.004
		Ni–*O*–Mg	12.1 ± (0.5)	2.98 ± (0.005)	0.012	
		Ni–*O*–Al	6.5 ± (3.0)	2.66 ± (0.041)	0.005	
	$Ni_{0.3}Mg_{3.7}AlO$	Ni–O	6.0 ± (0.2)	2.11 ± (0.002)	0.005	0.001
		Ni–*O*–Mg	12.2 ± (0.6)	2.98 ± (0.002)	0.012	
		Ni–*O*–Al	6.5 ± (3.4)	2.77 ± (0.026)	0.023	
	$Ni_{0.4}Mg_{3.8}AlO$	Ni–O	6.0 ± (0.7)	2.06 ± (0.005)	0.005	0.015
		Ni–*O*–Mg	11.9 ± (1.1)	2.54 ± (0.008)	0.012	
		Ni–*O*–Al	7.7 ± (6.1)	2.59 ± (0.062)	0.015	
	$Ni_{0.5}Mg_{3.5}AlO$	Ni–O	6.2 ± (0.6)	2.08 ± (0.013)	0.008	0.019
		Ni–*O*–Mg	11.9 ± (1.1)	2.96 ± (0.007)	0.013	
		Ni–*O*–Al	8.3 ± (7.0)	2.58 ± (0.073)	0.010	

Ni/Mg ratio from 0.2/3.8 to 0.3/3.7, except for a little change in Ni–*O*–Al bond length from 2.66 to 2.77 Å. However, at a higher Ni ratio from 0.3 to 0.5, a decrease in both Ni–*O*–Al bond radius along with the increase in its coordination number are observed, possibly due to the Ni anti-site defect, caused by the Ni^{2+} substitution on the Al^{3+} sites [55]. Moreover, an increase in the coordination number of Ni–*O*–Al also indicates the formation of NiO clusters outside the LDO structure. Since, the Ni^{2+} is unable anymore to be inserted to stabilize the structure, the Al atoms move towards Ni sublattice, resulting in the increase of Ni–*O*–Al coordination number [55,56]. As a result, the formation of NiO clusters occurs on the Ni_xMg_yAlO lodges.

3.2. Physical properties

Table 3 gives the elemental composition of sandwiched AgO@SnO_2/ZSM-5 and $Ni_xMg_{4-x}AlO$-embedded AgO@SnO_2/ZSM-5 catalysts, whereas Table 4 shows the elemental compositions of the embedded catalysts and $Ni_xMg_{4-x}AlO$-LDO samples prepared separately using the same preparation condition. The LDO samples have a quite similar relative mole ratio to the expected mole ratio value. The Ni replacement in the Mg position of the LDO layers ranges from 5 to 12.5 %. For the embedded samples, the $Ni_xMg_{4-x}AlO$s, grown on the AgO@SnO_2/ZSM-5, have slightly-higher Ni/Mg ratios than those grown as themselves. It can be implied that at a low Ni/Mg ratio, Ni can replace more greatly in the Mg position of $Ni_xMg_{4-x}AlH$ when the LDHs were grown on AgO@SnO_2/ZSM-5. Table 4 also reveals that the weight percentage of $Ni_xMg_{4-x}AlO$ in all $Ni_xMg_{4-x}AlO$-embedded AgO@SnO_2/ZSM-5 catalysts ranges from 62 to 67 %, meaning that the amount of the $Ni_xMg_{4-x}AlO$ lodges is twice as much as that of the embedded AgO@SnO_2/ZSM-5.

The physical properties of the catalyst samples are summarized in Table 5. A decrease in surface area along with the increase of average pore size is observed when each component is added into H-ZSM-5 step by step of preparation. Furthermore, the pore size in the range of microporosity are increased from 8.2 to 15.2 Å after the encapsulation by $Ni_xMg_{4-x}AlO$. The increasing Ni/Mg ratio does not affect to the pore size and volume. However, an increase in surface area along with the Ni/Mg are observed. The acidity and basicity of the catalysts are also summarized in Table 5 from the TPD profiles in Figs. S4 and S5 of the supplementary documents. The parent H-ZSM-5 zeolite consists of two acid sites, weak and strong acid sites. The deposition of SnO_2 creates a new medium-strength acid site, and the deposition of AgO onto the SnO_2/ZSM-5 layer increases the total acidity and basicity of the catalyst samples. The embedment by $Ni_xMg_{4-x}AlO$ further enhances both the total acidity and basicity of the resulting embedded catalysts, which are clearly contributed from $Ni_xMg_{4-x}AlO$ lodges. Furthermore, the increases in both medium-strength and strong acid/basic sites indicate that the presence of $Ni_xMg_{4-x}AlO$ lodges helps to enhance and modify the acid and basic strength of the $Ni_xMg_{4-x}AlO$-embedded AgO@SnO_2/ZSM-5 catalysts.

Our research group previously investigated the acidity and basicity of the Mg_xAlO-LDO catalysts, and found that the catalysts contain acid sites, which consist of weak Brønsted acid sites, assigned to OH groups, and strong Lewis acid sites contributed from Al^{3+}-O^{2-} pairs [46]. Moreover, three basic sites were identified as (a) weak Brønsted basic site related to the OH^- groups, (b) the medium strength Lewis basic site associated with Mg^{2+}-O^{2-} pairs, (c) and strong Lewis basic site that is related to the isolated O^{2-}. Moreover, the phase transformation of $Ni_xMg_{4-x}AlH$ to $Ni_xMg_{4-x}AlO$ after calcination was reportedly found to increase both acid and basic sites of the catalysts [57]. LDHs are known to contain abundant weak Brønsted basic sites due to the presence of –OH groups in the structure. Upon calcination, the –OH groups were transformed, resulting in the formation of $M^{2+/3+}$-O^{2-} pairs (Mg^{2+}-O^{2-}, Ni^{2+}-O^{2-}, and Al^{3+}-O^{2-}) as well as isolated O^{2-} group that exhibited stronger acid and basic properties. From Table 5, the substitution of Ni into Mg–*O*–Al sites in Mg_4AlO markedly enhances the acid and basic strength of the catalysts because a new formation of the Ni–*O*–Al or Ni–*O*–Mg present in $Ni_xMg_{4-x}AlO$. Since the electronegativity of Ni is higher than that of Mg and Al (Mg < Al < Ni = 1.31 < 1.61 < 1.91), the Ni–*O*–Al bonding creates a new stronger Lewis acid site than that is formed by the Al^{3+}-O^{2-} pairs [44]. Substitution of Ni into the structure also increase the electron density around the oxygen which therefore creates a stronger Lewis basic site and increased the overall basicity of the catalyst. Based on the XPS, XANES and EXAFS analysis, the illustration of $Ni_xMg_{4-x}AlO$ lodges with their acid and basic sites can be depicted in Fig. 7. In summary, the thermal treatment of $Ni_xMg_{4-x}AlH$ on AgO@SnO_2/ZSM-5 resulted in a more diverse acid and basic sites. Even though some of the –OH groups still exist in the structure, the majority have been transformed, leading to the formation of $M^{2+/3+}$-O^{2-} pairs and isolated O^{2-} that exhibit stronger Lewis basic sites, resulting in the improvement the overall basicity of the $Ni_xMg_{4-x}AlO$-embedded AgO@SnO_2/ZSM-5 catalysts.

Table 3
Elemental composition of sandwiched AgO@SnO_2/ZSM-5 and NixMg4-xAlO-embedded AgO@SnO_2/ZSM-5 catalysts.

Sample	Elemental composition (% wt.)[a]			
	Ag	Sn	Si	Al
Sandwiched Core-Shell				
AgO@SnO_2/ZSM-5	23.6	24	17.1	1.09
$Ni_xMg_{4-x}AlO$-embedded AgO@SnO_2/ZSM-5				
$Ni_{0.2}Mg_{3.8}AlO$	23.4	24.0	17.6	1.1
$Ni_{0.3}Mg_{3.7}AlO$	22.7	23.2	17.1	1.01
$Ni_{0.4}Mg_{3.6}AlO$	23.0	23.8	16.9	1.03
$Ni_{0.5}Mg_{3.5}AlO$	22.9	23.1	16.5	1.05

[a] Determined using XRF.

Table 4
Elemental compositions of separately-prepared $Ni_xMg_{4-x}AlO$ lodges and $Ni_xMg_{4-x}AlO$-embedded $AgO@SnO_2/ZSM-5$ catalysts.

Sample	Relative mole ratio[a]	Si/Al mole ratio[a]	% wt. of $Ni_xMg_{4-x}AlO$ in composite catalysts[b]	Thickness[c] (μm)	% Replacement of Ni in Mg positions of LDO				
Name $Ni_xMg_{4-x}AlO$ Lodges	Form	Ni	Mg	Al				Expected	Observed
$Ni_{0.2}Mg_{3.8}AlO$	–	0.2	3.8	1	–	–	–	5	5
$Ni_{0.3}Mg_{3.7}AlO$	–	0.3	3.8	1	–	–	–	7.5	7.3
$Ni_{0.4}Mg_{3.6}AlO$	–	0.5	3.4	1	–	–	–	10	12.8
$Ni_{0.5}Mg_{3.5}AlO$	–	0.6	3.5	1	–	–	–	12.5	14.6
$Ni_xMg_{4-x}AlO$ on $AgO@SnO_2/ZSM-5$									
$Ni_{0.2}Mg_{3.8}AlO$	Partial embedment	0.3	4.1	1	15	62	4.6	5	6.8
$Ni_{0.3}Mg_{3.7}AlO$	Partial embedment	0.4	4.0	1	15	66	4.8	7.5	8.9
$Ni_{0.4}Mg_{3.6}AlO$	Full embedment	0.5	3.9	1	15	65	5.0	10	11.4
$Ni_{0.5}Mg_{3.5}AlO$	Full embedment	0.7	3.9	1	15	67	5.1	12.5	15.2

[a] Determined by XRF.
[b] Calculated from $\frac{(Weight\ of\ NixMg1-xAlO)*100}{Weight\ of\ NixMg1-xAlO+Weight\ of\ AgO@SnO2/ZSM-5}$.
[c] Estimated from SEM/TEM images.

Table 5
Physical and chemical properties of $AgO@SnO_2/ZSM-5$ core and $Ni_xMg_{4-x}AlO$-embedded $AgO@SnO_2/ZSM-5$ catalysts.

Samples		S_{BET} (m^2/g)[a]	Pore Volume (cc/g)[b]	Average Pore Diameter (Å)[b]	Total Acidity (mmol/g)[c]	Total Basicity (mmol/g)[d]
Name Core	Form					
H-ZSM-5	–	356.4	0.26	5.6	0.575	0.260
$SnO_2/ZSM-5$	–	195.3	0.19	7.5	0.197	0.441
$AgO@SnO_2/ZSM-5$	–	93.4	0.17	8.2	0.747	0.672
$Ni_xMg_{4-x}AlO$ LDOs prepared separately						
$Ni_{0.2}Mg_{3.8}AlO$	–	106.9	0.34	38.2	0.985	1.063
$Ni_{0.3}Mg_{3.7}AlO$	–	114.3	0.33	38.2	1.188	1.313
$Ni_{0.4}Mg_{3.6}AlO$	–	120.8	0.34	38.2	0.955	1.051
$Ni_{0.5}Mg_{3.5}AlO$	–	134.5	0.34	38.2	1.158	1.227
$Ni_xMg_{4-x}AlO$ on $AgO@SnO_2/ZSM-5$						
$Ni_{0.2}Mg_{3.8}AlO$	Partial embedment	41.2	0.25	15.2	0.925	2.273
$Ni_{0.3}Mg_{3.7}AlO$	Partial embedment	47.1	0.23	15.2	1.012	2.392
$Ni_{0.4}Mg_{3.6}AlO$	Complete embedment	59.4	0.25	15.2	0.851	2.122
$Ni_{0.5}Mg_{3.5}AlO$	Complete embedment	68.5	0.25	15.2	0.992	2.437

[a] Determined using BET.
[b] Determined using BJH method.
[c] Determined using NH_3-TPD.
[d] Determined using CO_2-TPD.

3.3. Catalytic activity

The catalytic activity of $Ni_xMg_{4-x}AlO$-embedded $AgO/SnO_2@ZSM-5$ catalysts was investigated using glycerol as the feed at 180 °C for 4 h of residence time in order to study the roles of $AgO@SnO_2/ZSM-5$ clusters, and $Ni_xMg_{4-x}AlO$ lodges at various Ni/Mg ratios on the glycerol conversion.

3.3.1. Catalytic activity of $Ni_xMg_{4-x}AlO$ lodges as catalysts

The activity of $Ni_xMg_{4-x}AlO$ lodges separately tested as catalysts is shown in Fig. 8. It is revealed that without any catalyst, the conversion of glycerol is only 7.6 %; however, when a $Ni_xMg_{4-x}AlO$ was employed as a catalyst, the conversion starts to increase. At 5.0

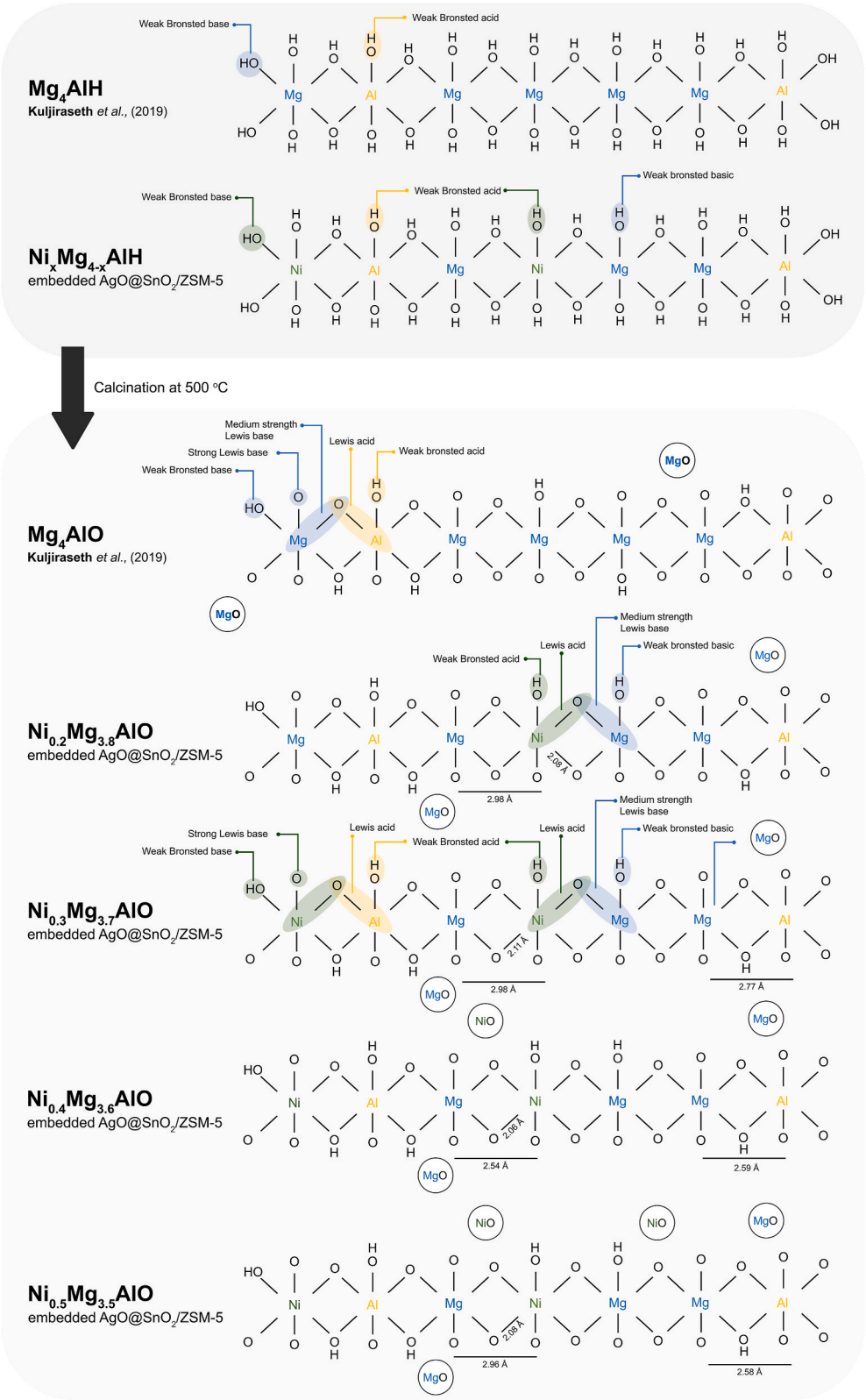

Fig. 7. Illustration of the layered structure of the $Ni_xMg_{4-x}AlO$ on $AgO@SnO_2$/ZSM-5 at various Ni/Mg ratios.

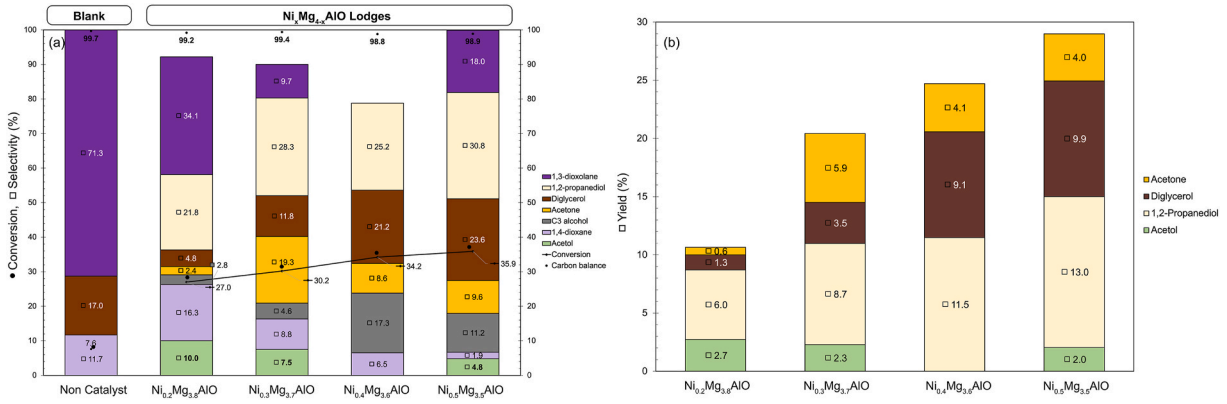

Fig. 8. (a) Glycerol conversion and product selectivity, and (b) Yield of selected products over pure $Ni_xMg_{4-x}AlO$ lodges separately tested as catalysts.

% Ni replacement, the $Ni_xMg_{4-x}AlO$ can convert 27.0 % glycerol. After that, the conversion is gradually increasing from 27.0% to 35.9 % with the increase of %Ni replacement from 5% to 14.6 %. Therefore, it is observed that the conversion of glycerol can be significantly affected by the Ni/Mg ratio of the $Ni_xMg_{4-x}AlO$. Based on Fig. 8(a), the non-catalytic reaction does not show much variety of the products. The selectivity only points towards the formation of 71.3 % dioxolane, 17.0 % diglycerol, and 11.7 % dioxane, indicating that the acetalization is highly favored, forming dioxolane as a major product with other co-products such as dioxane and diglycerol. The use of all $Ni_xMg_{4-x}AlO$s shows a wider spectrum of products with the major production of 1,2-propanediol. The selectivity towards 1,2-propanediol is gradually increasing with the increasing Ni/Mg ratio. Namely, at 5.0 % Ni replacement, the selectivity of 1,2-propanediol is 21.8 %, and it goes up to 37.1 % at 14.6 % Ni replacement. It is also found that other dominant products are dioxolanes, dioxanes, acetol, acetone, and alcohols, whose selectivity is varied with Ni/Mg ratio. Moreover, no lactic acid formation is observed. The yield of selected products are shown in Fig. 8(b). The highest yield of acetol is observed at the lowest %Ni replacement (5.0 %). Increasing Ni/Mg ratio results in a decrease of acetol yield along with an increase of 1,2-propanediol yield, which shows the presence of Ni species is attributed to the further conversion of acetol, forming 1,2-propanediol as a desired product.

Conclusively, it is found that the use of $Ni_xMg_{4-x}AlO$ as a catalyst does not only markedly increase the catalytic activity, but also affects the selectivity of the products. Without using any catalyst, the production moves majorly towards the formation of dioxolane groups, when a $Ni_xMg_{4-x}AlO$ is involved, the selectivity of dioxolanes is suppressed, resulting in a wider product distribution. The presence of Ni inside $Ni_xMg_{4-x}AlO$ drives the reaction towards the formation of 1,2- propanediol; namely, 1,2-propanediol yield is enhanced with the increasing %Ni replacement.

Based on the original hypothesis, acetol was expected to form as the major product, $Ni_xMg_{4-x}AlO$ as catalysts, but the LDOs themselves have a higher ability to form all the way to 1,2-propanediol with acetol formed as an intermediate. According to Scheme 1, glycerol conversion to 1,2-propanediol can possibly occur via two pathways; namely, (1) the first one involves with the dehydration of glycerol to acetol, followed by hydrogenation of acetol to 1,2-propanediol, or (2) through the glycerol dehydrogenation to glyceraldehyde, followed by dehydration of glyceraldehyde to 2-hydroxypropenal, and then to 1,2-propanediol through the hydrogenation of 2-hydroxypropenal [58,59]. Based on the results in Fig. 8(b), acetol, an intermediate from hydrogenolysis of glycerol, is observed with the decreasing yield along with the increase of 1,2-propanediol yield at a higher Ni ratio, meaning that 1,2-propanediol is produced over the $Ni_xMg_{4-x}AlO$ via the glycerol hydrogenolysis driven by Lewis acid sites. The gradual increase of 1,2-propanediol yield with the increasing Ni content implies that the Ni sites also drive the hydrogenation reaction of glycerol to 1,2-propanediol. In fact, the formation of 1,2-propanediol via acetol hydrogenation requires H_2; however, no any external H_2 was added in the experiments, meaning

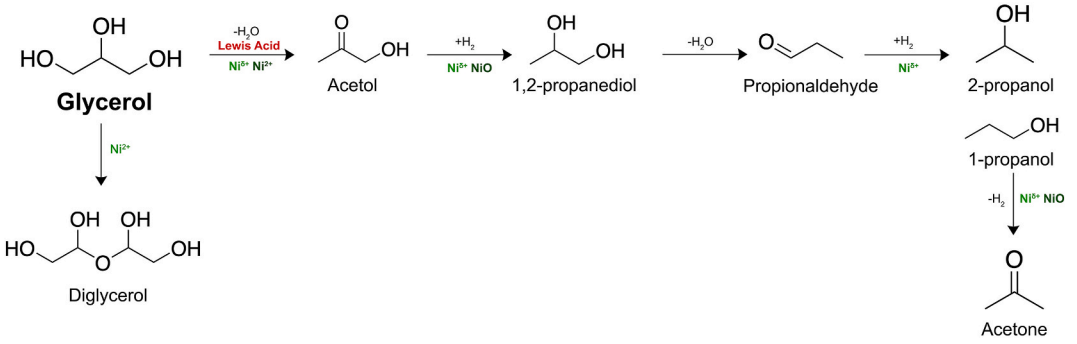

Fig. 9. Proposed influences of Ni sites in $Ni_xMg_{4-x}AlO$ lodges on glycerol conversion pathways.

that the *in-situ* H_2 is formed through glycerol reforming or the dehydrogenation of glycerol, resulting in the increase of 1,2-propanediol yield. In addition, the acetol yield appears to decrease with the increasing Ni/Mg ratio, and the higher yield of acetone, is evidently detected, meaning the Ni sites also promote the dehydration of 1,2-propanediol. The increases in selectivity and yield towards diglycerol with the Ni content are also observed in Fig. 8. The oligomerization of glycerol, or condensation between two glycerol molecules, forming diglycerol was reported to occur on with the higher basic or acid Lewis sites [59]. Hence, a higher Ni/Mg ratio is associated with the higher basic or Lewis acid sites of the LDOs, resulting in a higher selectivity and yield of diglycerol. The similar results were also reported on a higher Ni/Mg ratio of Ni-mixed oxide catalysts that enhanced the formation of diglycerol [59]. Moreover, Fig. 8(b) also confirms that $Ni_xMg_{4-x}AlO$ are able to produce acetol as a product, but acetol seems to be further converted into 1,2-propanediol, and the yield of 1,2-propanediol increases with the increase in Ni/Mg ratio. In conclusion, the influences of Ni in the $Ni_xMg_{4-x}AlO$ are on (1) the hydrogenolysis of glycerol, (2) glycerol oligomerization, and (3) glycerol reforming, as illustrated in Fig. 9.

3.3.2. *Catalytic activity of $Ni_xMg_{4-x}AlO$-embedded AgO/SnO_2@ZSM-5 catalysts*

The catalytic activity of $Ni_xMg_{4-x}AlO$-embedded AgO/SnO_2@ZSM-5 catalysts is exhibited in Fig. 10 in comparison with that of $AgO@SnO_2$/ZSM-5 clusters and $Ni_xMg_{4-x}AlO$ as benchmarks, and it can be seen that $AgO@SnO_2$/ZSM-5 as itself gives a much higher glycerol conversion (82.6 %) than any of $Ni_xMg_{4-x}AlO$. For the $Ni_xMg_{4-x}AlO$-embedded AgO/SnO_2@ZSM-5 catalysts, the embedment of $AgO@SnO_2$/ZSM-5 by the $Ni_xMg_{4-x}AlO$ lodges results in a remarkedly-higher conversion of glycerol than that of $Ni_xMg_{4-x}AlO$, but slightly lower than that of $AgO@SnO_2$/ZSM-5. It implies that the $AgO@SnO_2$/ZSM-5 helps to enhance the catalytic activity of $Ni_xMg_{4-x}AlO$. In addition, the conversion increases gradually as the Ni/Mg ratio of the embedded catalysts increases from 67.7 % to 77.0 % at the % Ni replacement from 6.8 % to 15.2 %, which indicates that Ni species also play the same role on the catalytic activity as previously reported in the sole $Ni_xMg_{4-x}AlO$.

Fig. 10 exhibits that the $AgO@SnO_2$/ZSM-5 produces 17.4 % selectivity of monoacetin as a major product together with 6.8 % lactic acid selectivity. Other side products are also formed in the products; for instances, 13.6 % 1,3-dioxolane, and 12.4 % 1,2-propanediol. The embedment of $AgO@SnO_2$/ZSM-5 in $Ni_xMg_{4-x}AlO$ lodges results in a wider spectrum of products. Particularly, when the $Ni_xMg_{4-x}AlO$-embedded $AgO@SnO_2$/ZSM-5 are employed, the selectivity moves towards the formation of 1,2-propanediol as a major product. The highest 44.4 % selectivity of 1,2-propanediol is also achieved at the lowest Ni/Mg ratio (6.8 % Ni replacement). Although the 1,2-propanediol yield is slightly dropped first at a lower Ni/Mg ratio, the increasing Ni/Mg ratio results in a gradual increase of 1,2-propanediol yield as shown in Table 6.

Earlier, Fig. 8 shows that all $Ni_xMg_{4-x}AlO$ are not capable of producing lactic acid. However, the incorporation of $Ni_xMg_{4-x}AlO$ onto $AgO@SnO_2$/ZSM-5 makes the $Ni_xMg_{4-x}AlO$-embedded $AgO@SnO_2$/ZSM-5 catalysts to be able to produce lactic acid with the highest 13.1 % selectivity at the lowest Ni/Mg ratio (6.8 % Ni replacement). Then, the selectivity eventually decreases along with an increase in the Ni/Mg ratio. A similar finding was also reported on $Pt_mNi_nO_x/TiO_2$ catalysts, which the decrease in lactic acid selectivity was observed with the increasing Ni content [55]. In summary, the presence of $AgO@SnO_2$/ZSM-5 in the $Ni_xMg_{4-x}AlO$-embedded $AgO@SnO_2$/ZSM-5 catalysts helps to drive all reactions toward the lactic acid formation. Table 6 shows that $AgO@SnO_2$/ZSM-5 clusters itself can form 5.4 % yield of lactic acid. An increase in lactic acid yield is observed in all the sandwiched shell@core catalysts, and the highest 8.7 % lactic acid yield is achieved at the Ni/Mg ratio of 0.2/3.8 (6.8 % Ni replacement). At a higher Ni/Mg ratio, the formation of lactic acid is suppressed, with the reasons that could be explained as follows. In the previous section, the presence of Ni species was found to drive the *in-situ* H_2 production from glycerol reforming reaction and/or the dehydrogenation of glycerol. Hence, at a Ni ratio higher than 0.3, the presence of NiO clusters (Fig. 10) makes the catalysts more selectively produce 1,2-propanediol rather than lactic acid. Moreover, at a higher ratio of Ni (0.4 and 0.5), the LDOs fully cover $AgO@SnO_2$/ZSM-5 cluster, and prevent acetol from contacting with the $AgO@SnO_2$/ZSM-5 clusters, resulting in a lower yield of lactic acid. This is also proven by the increase of acetol yield when the ratio of Ni/Mg is increasing. Furthermore, the formation of acetic acid and monoacetin also indicate the further oxidation of lactic acid, which impacts to the overall yield of lactic acid.

3.4. *Influences of $Ni_xMg_{4-x}AlO$-embedded $AgO@SnO_2$/ZSM-5 catalysts on glycerol pathways*

The influences of the catalysts on the glycerol conversion are depicted in Fig. 11. Initially, the $Ni_xMg_{4-x}AlO$ lodges provide Lewis acid sites to drive the glycerol dehydration to acetol, and then the metal sites further drive the hydrogenation acetol to 1,2-propanediol. Simultaneously, the presence of Ni drives the *in-situ* H_2 production from the glycerol reforming and/or from the dehydrogenation of glycerol. Subsequently, the presence of silver oxide and tin oxide on $AgO@SnO_2$/ZSM-5 clusters allows the clusters to produce lactic acid in the liquid product with the following explanations. The presence of AgO is found to govern the oxidation of acetol to pyruvaldehyde, and the presence of Lewis acid sites on SnO_2/ZSM-5 drives the lactic acid formation via Cannizaro reaction. However, due to the high amounts of AgO and SnO_2, the further oxidation of lactic acid is also occurred, resulting in the formation of acetic acid and monoacetin.

Obviously, the products are formed from the synergy between the $Ni_xMg_{4-x}AlO$ lodges and $AgO@SnO_2$/ZSM-5 clusters since the lactic acid production on a sandwiched shell@core catalyst is higher than on the $AgO@SnO_2$/ZSM-5 clusters or on the $Ni_xMg_{4-x}AlO$ only, proving that the presences of $Ni_xMg_{4-x}AlO$ lodges help to enhance the acetol formation that leads to higher lactic acid yield. Therefore, the embedded shell@core catalysts structure is essentially required to form a high yield of lactic acid in the cases when no addition of an alkaline, an oxidizing agent, and H_2 gas is required. Table 7 exhibits the catalytic performance of one of our catalysts, $Ni_{0.2}Mg_{3.8}AlO$-embedded $AgO@SnO_2$/ZSM-5, in comparison with that of other previously-reported catalysts for glycerol valorization to lactic acid and 1,2-propanediol. It can be observed that our catalyst gives a significantly-high glycerol conversion of 67.7 % from

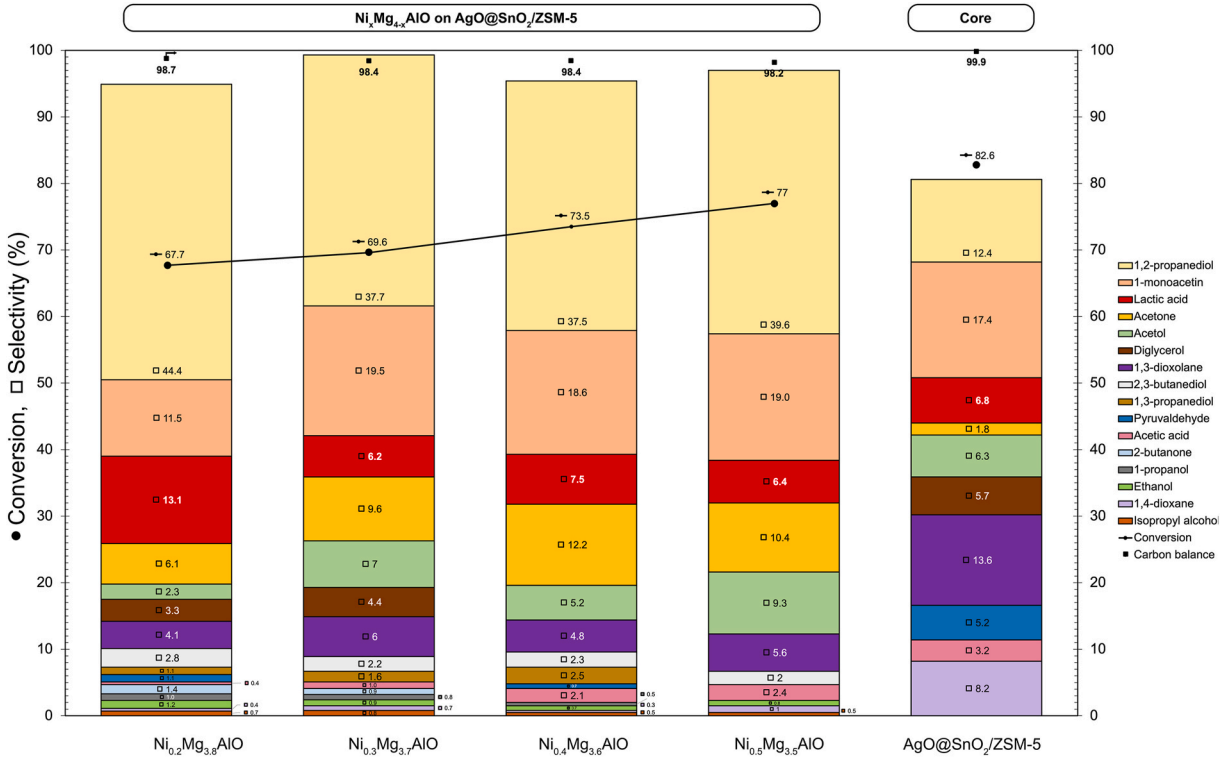

Fig. 10. Glycerol conversion and selectivity of products over AgO@SnO$_2$/ZSM-5 and Ni$_x$Mg$_{4-x}$AlO-embedded AgO@SnO$_2$/ZSM-5 catalysts.

Table 6
%Yield of selected products over Ni$_x$Mg$_{4-x}$AlO-embedded AgO@SnO$_2$/ZSM-5 catalysts.

Samples		Conversion (%)	% Yield of selected product					
Name	Form		LA	1,2-PDO	AC	ACN	AA	PYD
Individual components								
Ni$_{0.2}$Mg$_{3.8}$AlO	LDO	27.0	–	5.9	2.7	0.7	–	–
Ni$_{0.3}$Mg$_{3.7}$AlO	LDO	30.2	–	8.5	2.3	5.8	–	–
Ni$_{0.4}$Mg$_{3.6}$AlO	LDO	34.2	–	8.6	0.0	2.9	–	–
Ni$_{0.5}$Mg$_{3.5}$AlO	LDO	35.9	–	11.1	1.7	3.4	–	–
AgO@SnO$_2$/ZSM-5	Sandwiched core-shell	82.6	5.6	10.2	5.2	1.5	2.6	4.3
Ni$_x$Mg$_{4-x}$AlO on AgO@SnO$_2$/ZSM-5								
Ni$_{0.2}$Mg$_{3.8}$AlO	Partial embedment	67.7	9.1	30.1	1.6	4.1	0.3	0.7
Ni$_{0.3}$Mg$_{3.7}$AlO	Partial embedment	69.6	4.3	26.2	4.9	6.7	0.7	–
Ni$_{0.4}$Mg$_{3.6}$AlO	Full embedment	73.5	5.5	27.6	3.8	9.0	1.5	0.5
Ni$_{0.5}$Mg$_{3.5}$AlO	Full embedment	77.0	4.9	30.5	7.2	8.0	1.9	–

Note: LA: Lactic Acid; 1,2-PDO: 1,2-Propanediol; AC: Acetol; ACN: Acetone; AA: Acetic Acid; PYD: Pyruvaldehyde.

even 99.9 % pure glycerol used as the feed, whereas the catalysts reported in the other articles gave a higher conversion, but only a feed with an extremely-low glycerol concentration was employed. In addition, although our catalyst still cannot give a higher selectivity of lactic acid than the others in comparison, it can yield a considerable amount of lactic acid and also 1,2-propanediol without the addition of an alkaline, an oxidizing agent, and H_2 gas at the atmospheric pressure. With more investigation and modification, the catalysts would possibly have a high potential to become more superior to produce lactic acid and 1,2-propanediol simultaneously.

4. Conclusions

In this work, the core-shell structured catalysts have been proven to be potential alternatives to simultaneously produce 1,2-propanediol and lactic acid from glycerol without the additional of either alkali or external H_2 gas. Based on the results, the Ni$_x$Mg$_{4-x}$AlO lodges influenced the hydrogenolysis reaction that led to the acetol and 1,2-propanediol formation, whereas the AgO@SnO$_2$/ZSM-5 governed the oxidation-Cannizarro reaction that led to the formation of lactic acid. Either partial or complete embedment of Ni$_x$Mg$_{4-}$

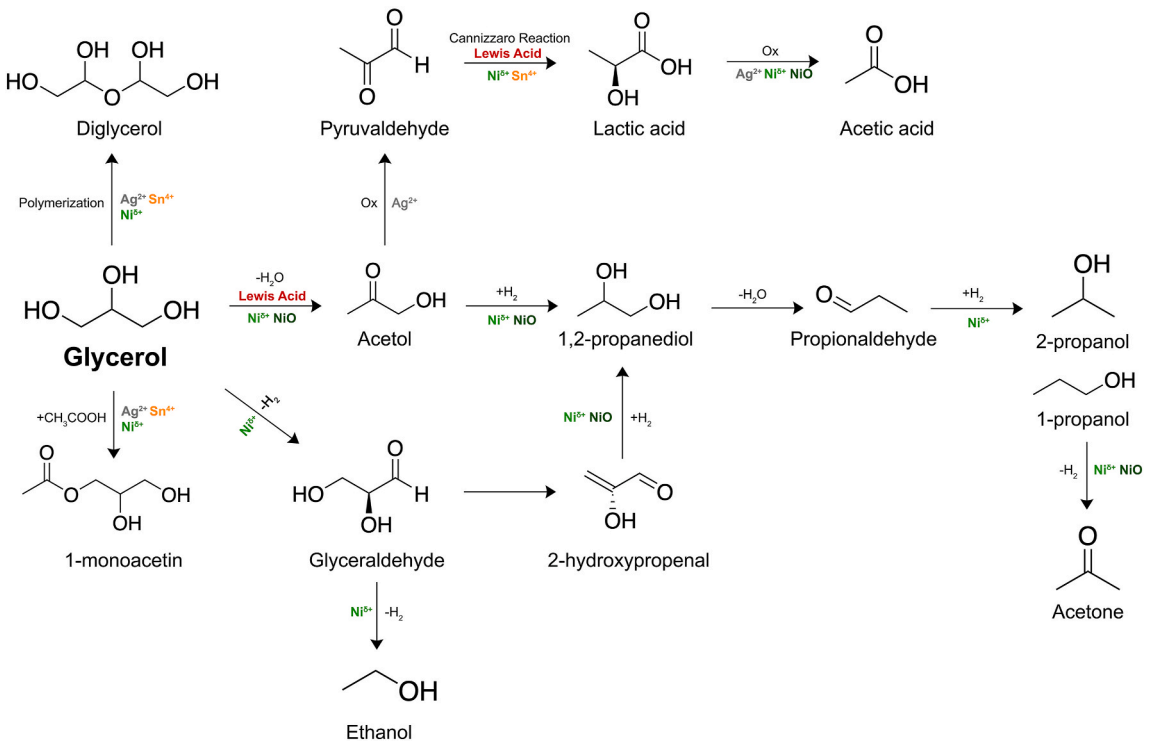

Fig. 11. Proposed influences of $Ni_xMg_{4-x}AlO$-embedded AgO/SnO_2@ZSM-5 catalysts and their components on glycerol valorization.

Table 7
Catalytic performance of the $Ni_{0.2}Mg_{3.8}AlO$-embedded $AgO@SnO_2$/ZSM-5 catalyst in comparison with that of other previously-reported catalysts for glycerol valorization to lactic acid and 1,2-propanediol.

Catalyst	Conversion of glycerol (%)	Selectivity of two major products (%)		Glycerol concentration in feed	NaOH/ Glycerol Ratio	Temp (^{o}C)	Time (h)	External Gas (MPa)	Ref.
		Lactic Acid	1,2-PDO						
$Ni_{0.2}Mg_{3.8}AlO$-embedded $AgO@SnO_2$/ZSM5	67.7	13.1	44.4	Pure glycerol (99.9 %)	–	180	4	–	This work
$CuAu_2$	99.0	93.8	0.3	2 M Glycerol (aq)	1.1:1.0	200	2	–	[19]
Pt/ZSM-11	~65.0	53.5	–	0.25 Glycerol (aq)	2.0:1.0	100	4	–	[60]
$[Ir(COD)(IMe)_2]BF_4$	94.0	96.6	1.3	~0.1 M Glycerol (aq)	1.1*:1	130	24	–	[8]
$Cu_{0.4}/Zn_{0.6}Mg_{5.0}Al_2O_{8.6}$	78.2	99.3	–	0.02 M Glycerol (aq)	–	180	10	$2.0H_2$	[61]
Reduced $Cu_{0.3}Mg_{1.7}AlO$	58.3	6.0	89.5	80 % Glycerol in ethanol	–	180	–	–	[18]

$_xAlO$ lodges onto the $AgO@SnO_2$/ZSM-5 clusters resulted in a better yield of 1,2-propanediol and lactic acid than its individual catalyst component. The presence of Ni^{2+} enhanced the formation of 1,2-propanediol by driving the *in-situ* H_2 production via glycerol reforming. Especially, at the lowest Ni/Mg ratio where the embedment was observed, the highest 8.7 % yield of lactic acid was obtained. Moreover, increasing Ni/Mg ratio made the $Ni_xMg_{4-x}AlO$ lodges fully cover the $AgO@SnO_2$/ZSM-5 clusters, resulting in the lower lactic acid yield, and the high amount of Ni^{2+} could also drive the further oxidation of lactic acid to acetic acid and monoacetin at a higher Ni ratio.

CRediT authorship contribution statement

Darine Denala: Writing – original draft, Resources, Methodology, Investigation, Formal analysis, Data curation. **Wutthikrai Busayaporn:** Writing – review & editing, Validation, Software, Resources, Formal analysis. **Wantana Klysubun:** Validation, Supervision, Software, Resources. **Sirirat Jitkarnka:** Writing – review & editing, Visualization, Validation, Supervision, Resources,

Project administration, Funding acquisition, Formal analysis, Data curation, Conceptualization.

Declaration of competing interest

The authors declare that they have no known competing financial interests or personal relationships that could have appeared to influence the work reported in this paper.

6. Acknowledgements

The authors gratefully acknowledge the mutual supports from Fundamental Fund of Fiscal Years 2022 (CU_FRB65_bcg(30)_200_63_02) and 2023 (BCG66630025) from Chulalongkorn University, Center of Excellence for Petrochemical and Materials Technology, and ASEAN Scholarship from Chulalongkorn University, THAILAND.

Appendix A. Supplementary data

Supplementary data to this article can be found online at https://doi.org/10.1016/j.heliyon.2024.e30325.

References

[1] IEA, Renewables 2021, 2021.
[2] A.A. Abdul Raman, H.W. Tan, A. Buthiyappan, Two-step purification of glycerol as a value added by product from the biodiesel production process, Front. Chem. 7 (2019) 774.
[3] A.L. Chun Minh, S.P. Samudrala, S. Bhattacharya, Valorisation of glycerol through catalytic hydrogenolysis routes for sustainable production of value-added C3 chemicals: current and future trends, Sustain. Energy Fuels 6 (2022) 596–639.
[4] C. Dai, L. Sun, H. Liao, B. Khezri, R.D. Webster, A.C. Fisher, Z.J. Xu, Electrochemical production of lactic acid from glycerol oxidation catalyzed by AuPt nanoparticles, J. Catal. 356 (2017) 14–21.
[5] N. Razali, A.Z. Abdullah, Production of lactic acid from glycerol via chemical conversion using solid catalyst: a review, Appl. Catal., A 543 (2017) 234–246.
[6] C. Wang, X. Zhang, J. Li, X. Qi, Z. Guo, H. Wei, H. Chu, Gold nanoparticles on nanosheets derived from layered rare-earth hydroxides for catalytic glycerol-to-lactic acid conversion, ACS Appl. Mater. Interfaces 13 (1) (2021) 522–530.
[7] C. Crotti, E. Farnetti, Selective oxidation of glycerol catalyzed by iron complexes, J. Mol. Catal. Chem. 396 (2015) 353–359.
[8] L.S. Sharninghausen, J. Campos, M.G. Manas, R.H. Crabtree, Efficient selective and atom economic catalytic conversion of glycerol to lactic acid, Nat. Commun. 5 (2014) 5084.
[9] L. Shen, X. Zhou, C. Zhang, H. Yin, A. Wang, C. Wang, Functional characterization of bimetallic CuPdx nanoparticles in hydrothermal conversion of glycerol to lactic acid, J. Food Biochem. 43 (2019) e12931.
[10] L. Shen, Z. Yu, D. Zhang, H. Yin, C. Wang, A. Wang, Glycerol valorization to lactic acid catalyzed by hydroxyapatite-supported palladium particles, J. Chem. Technol. Biotechnol. 94 (2019) 204–215.
[11] A. Wang, Q. Xu, H. Yin, Synthesis of lactic acid starting from glycerol catalyzed by CaO-supported CuO and metallic Cu catalysts in Ca(OH)2 aqueous solution, React. Kinet. Mech. Catal. 135 (2022) 3205–3221.
[12] C.-Q. Deng, J. Deng, Y. Fu, Manganese-catalysed dehydrogenative oxidation of glycerol to lactic acid, Green Chem. 24 (2022) 8477–8483.
[13] H. Yin, C. Zhang, H. Yin, D. Gao, L. Shen, A. Wang, Hydrothermal conversion of glycerol to lactic acid catalyzed by Cu/hydroxyapatite, Cu/MgO, and Cu/ZrO_2 and reaction kinetics, Chem. Eng. J. (Lausanne) 288 (2016) 332–343.
[14] W. Oberhauser, C. Evangelisti, C. Tiozzo, F. Vizza, R. Psaro, Lactic acid from glycerol by ethylene-stabilized platinum-nanoparticles, ACS Catal. 6 (2016) 1671–1674.
[15] S. Torres, R. Palacio, D. Lopez, Support effect in Co3O4-based catalysts for selective partial oxidation of glycerol to lactic acid, Appl. Catal. Gen. 621 (2021) 118199.
[16] G.M. Lari, R. García-Muelas, C. Mondelli, N. López, J. Pérez-Ramírez, Glycerol oxidehydration to pyruvaldehyde over silver-based catalysts for improved lactic acid production, Green Chem. 18 (2016) 4682–4692.
[17] H. Zhao, L. Zheng, X. Li, P. Chen, Z. Hou, Hydrogenolysis of glycerol to 1,2-propanediol over Cu-based catalysts: a short review, Catal. Today 355 (2020) 84–95.
[18] J. Kuljiraseth, T. Kumpradit, T. Leungcharoenwattana, Y. Poo-arporn, S. Jitkarnka, Integrated glycerol- and ethanol-based chemical synthesis routes using Cu–Mg–Al LDH-derived catalysts without external hydrogen: intervention of bio-ethanol co-fed with glycerol, Renew. Energy 156 (2020) 975–985.
[19] N. Dimitratos, J.A. Lopez-Sanchez, S. Meenakshisundaram, J.M. Anthonykutty, G. Brett, A.F. Carley, S.H. Taylor, D.W. Knight, G.J. Hutchings, Selective formation of lactate by oxidation of 1,2-propanediol using gold palladium alloy supported nanocrystals, Green Chem. 11 (2009) 1209–1216.
[20] V.V. Torbina, A.A. Vodyankin, S. Ten, G.V. Mamontov, M.A. Salaev, V.I. Sobolev, O.V. Vodyankina, Ag-based catalysts in heterogeneous selective oxidation of alcohols: a review, Catal. 8 (2018).
[21] L. Shen, X. Zhou, A. Wang, H. Yin, H. Yin, W. Cui, Hydrothermal conversion of high-concentrated glycerol to lactic acid catalyzed by bimetallic CuAux (x = 0.01–0.04) nanoparticles and their reaction kinetics, RSC Adv. 7 (2017) 30725–30739.
[22] J. Xu, H. Zhang, Y. Zhao, B. Yu, S. Chen, Y. Li, L. Hao, Z. Liu, Selective oxidation of glycerol to lactic acid under acidic conditions using AuPd/TiO2 catalyst, Green Chem. 15 (2013).
[23] S. Sato, M. Akiyama, R. Takahashi, T. Hara, K. Inui, M. Yokota, Vapor-phase reaction of polyols over copper catalysts, Appl. Catal., A 347 (2008) 186–191.
[24] A. Alhanash, E.F. Kozhevnikova, I.V. Kozhevnikov, Gas-phase dehydration of glycerol to acrolein catalysed by caesium heteropoly salt, Appl. Catal., A 378 (2010) 11–18.
[25] S. Célerier, S. Morisset, I. Batonneau-Gener, T. Belin, K. Younes, C. Batiot-Dupeyrat, Glycerol dehydration to hydroxyacetone in gas phase over copper supported on magnesium oxide (hydroxide) fluoride catalysts, Appl. Catal., A 557 (2018) 135–144.
[26] N.K. Mishra, P. Kumar, V.C. Srivastava, U.L. Štangar, Synthesis of Cu-based catalysts for hydrogenolysis of glycerol to 1,2-propanediol with in-situ generated hydrogen, J. Environ. Chem. Eng. 9 (2021) 105263.
[27] J. Mazarío, P. Concepción, M. Ventura, M.E. Domine, Continuous catalytic process for the selective dehydration of glycerol over Cu-based mixed oxide, J. Catal. 385 (2020) 160–175.
[28] S. Mészáros, J. Halász, Z. Kónya, P. Sipos, I. Pálinkó, Reconstruction of calcined MgAl- and NiMgAl-layered double hydroxides during glycerol dehydration and their recycling characteristics, Appl. Clay Sci. 80–81 (2013) 245–248.
[29] R.B. Mane, C.V. Rode, Simultaneous glycerol dehydration and in situ hydrogenolysis over Cu–Al oxide under an inert atmosphere, Green Chem. 14 (2012).

[30] I. Gandarias, P.L. Arias, S.G. Fernández, J. Requies, M. El Doukkali, M.B. Güemez, Hydrogenolysis through catalytic transfer hydrogenation: glycerol conversion to 1,2-propanediol, Catal. Today 195 (2012) 22–31.

[31] M. Checa, F. Auneau, J. Hidalgo-Carrillo, A. Marinas, J.M. Marinas, C. Pinel, F.J. Urbano, Catalytic transformation of glycerol on several metal systems supported on ZnO, Catal. Today 196 (2012) 91–100.

[32] H.J. Cho, C.-C. Chang, W. Fan, Base free, one-pot synthesis of lactic acid from glycerol using a bifunctional Pt/Sn-MFI catalyst, Green Chem. 16 (2014) 3428–3433.

[33] M. Tao, Z. Dan, H. Guan, G. Huang, X. Wang, Designation of highly efficient catalysts for one pot conversion of glycerol to lactic acid, Sci. Rep. 6 (2016) 29840.

[34] S. Das, J. Pérez-Ramírez, J. Gong, N. Dewangan, K. Hidajat, B.C. Gates, S. Kawi, Core–shell structured catalysts for thermocatalytic, photocatalytic, and electrocatalytic conversion of CO_2, Chem. Soc. Rev. 49 (2020) 2937–3004.

[35] L. Zheng, X. Li, W. Du, D. Shi, W. Ning, X. Lu, Z. Hou, Metal-organic framework derived Cu/ZnO catalysts for continuous hydrogenolysis of glycerol, Appl. Catal. B Environ. 203 (2017) 146–153.

[36] Z. Xiu, H. Wang, C. Cai, C. Li, L. Yan, C. Wang, W. Li, H. Xin, C. Zhu, Q. Zhang, Q. Liu, L. Ma, Ultrafast glycerol conversion to lactic acid over magnetically recoverable NiNiOx@C catalysts, Ind. Eng. Chem. Res. 59 (2020) 9912–9925.

[37] D.J. DenalaS, Identification of possible acetol conversion pathways to valuable bio-based chemicals using Ag/Sn-beta catalyst. The 27th PPC Symposium on Petroleum and Petrochemicals and Polymers and the 12th Research Symposium on Petrochemical and Materials TechnologyBangkok, Thailand, 2021.

[38] D. Denala, Glycerol conversion to lactic acid over AgO-promoted SnO2/zeolite catalysts. Petrochemical Technology, Chulalongkorn University, Bangkok, Thailand, 2021.

[39] S. Xia, W. Du, L. Zheng, P. Chen, Z. Hou, A thermally stable and easily recycled core shell Fe2O3@CuMgAl catalyst for hydrogenolysis of glycerol, Catal. Sci. Technol. 4 (2014) 912–916.

[40] W. Klysubun, P. Tarawarakarn, N. Thamsanong, P. Amonpattaratkit, C. Cholsuk, S. Lapboonrueng, S. Chaichuay, W. Wongtepa, Upgrade of SLRI BL8 beamline for XAFS spectroscopy in a photon energy range of 1–13 keV, Radiat. Phys. Chem. (2020) 175.

[41] B. Ravel, M. Newville, ATHENA, ARTEMIS, hephaestus: data analysis for X-ray absorption spectroscopy using IFEFFIT, J. Synchrotron Radiat. 12 (2005) 537–541.

[42] A. Debataraja, D.W. Zulhendri, B. Yuliarto, Hiskia Nugraha, B. Sunendar, Investigation of nanostructured SnO2 synthesized with polyol technique for CO gas sensor applications, Procedia Eng. 170 (2017) 60–64.

[43] B. Gauri, K. Vidya, S. Gadale -Dagade, S. Waghmode, Synthesis and Characterization of Ag/AgO nanoparticles as alcohol sensor, Res. J. Chem. Environ. 20 (2016).

[44] T. Leungcharoenwattana, S. Jitkarnka, Bio-based chemical production from glycerol conversion with ethanol co-feeding over Zr-promoted MgAl-layered double oxide catalysts: impact of zirconium location, J. Clean. Prod. 273 (2020) 123201.

[45] J. Kuljiraseth, A. Wangriya, J.M.C. Malones, W. Klysubun, S. Jitkarnka, Synthesis and characterization of AMO LDH-derived mixed oxides with various Mg/Al ratios as acid–basic catalysts for esterification of benzoic acid with 2-ethylhexanol, Appl. Catal. B Environ. 243 (2019) 415–427.

[46] J. Török, J. Halász, Z. Kónya, P. Sipos, I. Pálinkó, Mixed oxides without added noble metals derived from layered double hydroxides of the hydrotalcite type in the hydrodechlorination reaction of trichloroethylene, Catal. Lett. 147 (2017) 2910–2919.

[47] R. Dębek, M. Motak, D. Duraczyska, F. Launay, M.E. Galvez, T. Grzybek, P. Da Costa, Methane dry reforming over hydrotalcite-derived Ni–Mg–Al mixed oxides: the influence of Ni content on catalytic activity, selectivity and stability, Catal. Sci. Technol. 6 (2016) 6705–6715.

[48] H. Li, H. Wei, Y. Cui, R.-L. Sang, J.-L. Bu, Y.-N. Wei, J. Lin, J.-H. Zhao, Synthesis and characterisation of MgAl2O4 spinel nanopowders via nonhydrolytic sol–gel route, J. Ceram. Soc. Jpn. 125 (2017) 100–104.

[49] Y.N. Ko, Y.C. Kang, S.B. Park, Continuous one-pot synthesis of sandwich structured core–shell particles and transformation to yolk–shell particles, Chem comm 49 (2013) 3884–3886.

[50] Y.W. Tsai, B.J. Hwang, G. Ceder, H.S. Sheu, D.G. Liu, J.F. Lee, In-situ X-ray absorption spectroscopic study on variation of electronic transitions and local structure of LiNi1/3Co1/3Mn1/3O2 cathode material during electrochemical cycling, Chem. Mater. 17 (2005) 3191–3199.

[51] M.L. Baker, M.W. Mara, J.J. Yan, K.O. Hodgson, B. Hedman, E.I. Solomon, K- and L-edge X-ray absorption spectroscopy (XAS) and resonant inelastic X-ray scattering (RIXS) determination of differential orbital covalency (DOC) of transition metal sites, Coord. Chem. Rev. 345 (2017) 182–208.

[52] H.K.D. Nguyen, T.D. Nguyen, D.N. Hoang, D.S. Dao, T.T. Nguyen, L. Wanwisa, L.L. Hoang, X-ray absorption spectroscopies of Mg-Al-Ni hydrotalcite like compound for explaining the generation of surface acid sites, Kor. J. Chem. Eng. 34 (2016) 314–319.

[53] Y. Izumi, T. Shimizu, T. Kobayashi, K.-i. Aika, Nitrous oxide decomposition active site on Ni–MgO catalysts characterized by X-ray absorption fine structure spectroscopy, Chem comm (2000) 1053–1054.

[54] K. Asakura, Y. Iwasawa, H. Kuroda, EXAFS AND XANES STUDIES ON THE LOCAL STRUCTURES OF METAL IONS IN METAL DOPED MgO SYSTEMS, J. Phys. Colloq. 47 (1986).

[55] Y. Li, S. Chen, J. Xu, H. Zhang, Y. Zhao, Y. Wang, Z. Liu, Ni promoted Pt and Pd catalysts for glycerol oxidation to lactic acid, Clean: Soil, Air, Water 42 (2014) 1140–1144.

[56] M.S. Bailey, N.T. Wilson, C. Roberts, R.L. Johnston, Structures, stabilities and ordering in Ni-Al nanoalloy clusters, the European physical journal D - atomic, Molecular and Optical Physics 25 (2003) 41–55.

[57] W. Zhou, Q. Tao, J. Pan, J. Liu, J. Qian, M. He, Effect of basicity on the catalytic properties of Ni-containing hydrotalcites in the aerobic oxidation of alcohol, J. Mol. Catal. Chem. 425 (2016) 255–265.

[58] S.P. Samudrala, Glycerol transformation to value-added 1,3-propanediol production: a paradigm for a sustainable biorefinery process, glycerine production and transformation - an innovative platform for sustainable biorefinery and energy, in: M.B. Marco Frediani, Luca Rosi (Eds.), Glycerine Production and Transformation: an Innovative Platform for Sustainable Biorefinery and Energy, Intech Open, 2019.

[59] M. Aloui, J.A. Cecilia, R. Moreno-Tost, S.B. Ghorbel, M. Saïd Zina, E. Rodríguez-Castellón, Glycerol etherification towards selective diglycerol over mixed oxides derived from hydrotalcites: effect of Ni loading, J. Sol. Gel Sci. Technol. 97 (2021) 351–364.

[60] E. Diguilio, M.S. Renzini, L.B. Pierella, M.E. Domine, Conversion of glycerol to value added products in a semi-continuous batch reactor using noble metals supported on ZSM-11 zeolite, Nanomaterials 11 (2021) 1–19.

[61] S. Xia, R. Nie, L. Xiuyang, L. Wang, P. Chen, Z. Hou, Hydrogenolysis of glycerol over Cu0.4/Zn5.6−xMgxAl2O8.6 catalysts: the role of basicity and hydrogen spillover, J. Catal. 296 (2012) 1–11.